AGU PUBLICATIONS

JGR

Journal of Geophysical Research: Atmospheres

RESEARCH ARTICLE
10.1002/2016JD024769

Key Points:
- The changes in Arctic regional sea ice extents (RSIEs) are quantified for the period 1979-2014
- Arctic RSIE exhibits marked differences in trends and interannual variability in different regions
- RSIEs in different regions are associated with distinct patterns of winter atmospheric variability

Correspondence to:
H. W. Chen,
hans.chen@psu.edu

Citation:
Chen, H. W., R. B. Alley, and F. Zhang (2016), Interannual Arctic sea ice variability and associated winter weather patterns: A regional perspective for 1979–2014, *J. Geophys. Res. Atmos.*, *121*, 14,433–14,455, doi:10.1002/2016JD024769.

Received 6 JAN 2016
Accepted 26 NOV 2016
Accepted article online 9 DEC 2016
Published online 27 DEC 2016

Interannual Arctic sea ice variability and associated winter weather patterns: A regional perspective for 1979–2014

Hans W. Chen[1,2], Richard B. Alley[2,3], and Fuqing Zhang[1,2]

[1]Department of Meteorology and Atmospheric Science, Pennsylvania State University, University Park, Pennsylvania, USA, [2]Center for Advanced Data Assimilation and Predictability Techniques, Pennsylvania State University, University Park, Pennsylvania, USA, [3]Department of Geosciences, and Earth and Environmental Systems Institute, Pennsylvania State University, University Park, Pennsylvania, USA

Abstract Using Arctic sea ice concentration derived from passive microwave satellite observations in autumn and early winter over the 1979–2014 period, the Arctic region was objectively classified into several smaller regions based on the interannual sea ice variability through self-organizing map analyses. The trend in regional sea ice extent (RSIE) in each region was removed using an adaptive, nonlinear, and nonstationary method called Ensemble Empirical Mode Decomposition, which captures well the accelerating decline of Arctic RSIEs in recent decades. Although the linear trend in RSIE is negative in all regions in both seasons, there are marked differences in RSIE trends and variability between regions, with the largest negative trends found during autumn in the Beaufort Sea, the Barents-Kara Seas, and the Laptev-East Siberian Seas. Winter weather patterns associated with the nonlinearly detrended RSIEs show distinct features for different regions and tend to be better correlated with the autumn than early winter RSIE anomalies. Sea ice losses in the Beaufort Sea and the Barents-Kara Seas are both associated with a cooling of Eurasia, but in the former case the circulation anomaly is reminiscent of a Rossby wave train, whereas in the latter case the pattern projects onto the negative phase of the Arctic Oscillation. These results highlight the nonuniform changes in Arctic sea ice and suggest that regional sea ice variations may play a crucial role for the winter weather patterns.

1. Introduction

The sea ice in the Arctic has decreased drastically in recent decades [*Simmonds*, 2015], and there are indications that the decline is accelerating [*Comiso et al.*, 2008; *Stroeve et al.*, 2012a]. Arctic sea ice is sensitive to changes in the global climate system, partly owing to the many positive feedback mechanisms in the Arctic region; thus, variations in sea ice can be a critical indicator of climate change. Moreover, sea ice is a key player for the local Arctic climate system due to its influence on the surface albedo, heat, and moisture fluxes between the atmosphere and ocean, surface roughness, and ocean circulation [*Budikova*, 2009]. Decreased sea ice cover has been shown to play a leading role in Arctic amplification [*Screen and Simmonds*, 2010; *Walsh*, 2014], i.e., a larger warming trend observed in the Arctic region compared with lower latitudes.

There has been an increasing scientific interest in the variability and trends of Arctic sea ice cover due to its potential impact on midlatitude weather and climate. A growing number of studies have found links between decreased sea ice and anomalous weather patterns in the midlatitudes [see, e.g., *Cohen et al.*, 2014; *Vihma*, 2014]. *Francis and Vavrus* [2012] proposed that reduced sea ice and Arctic amplification lead to a reduction of the meridional geopotential height gradient, slower propagation of Rossby waves in the upper atmosphere, and increased amplitude of planetary waves, with possible consequences for the midlatitudes including slower moving weather systems and therefore more frequent extreme weather events. However, these proposed impacts of Arctic sea ice loss do not show up clearly in the short observational records and are sensitive to the methodology used to identify changes in weather and climate variability [*Barnes*, 2013]. Model simulations have so far produced relatively weak responses in midlatitude weather to decreased Arctic sea ice. The atmospheric signals are typically much smaller than the intrinsic variability of the atmosphere [e.g., *Alexander et al.*, 2004; *Screen et al.*, 2013]. Whereas the warming in the Arctic scales roughly linearly with the sea ice decline [*Chen et al.*, 2016], the simulated midlatitude atmospheric response exhibits large nonlinearity

[*Petoukhov and Semenov*, 2010; *Semenov and Latif*, 2015] and is not robust to linear changes in Arctic sea ice cover [*Chen et al.*, 2016].

Recent studies have found that the spatial pattern of sea ice variability may play an important role in determining whether, and how, Arctic sea ice anomalies impact midlatitude weather and climate. *Peings and Magnusdottir* [2014] used an atmospheric model to show that the midlatitude atmospheric response to sea ice loss is related to upward propagation of planetary waves. In their model simulations, a larger sea ice decrease did not necessarily translate to a larger midlatitude response, which could be partially explained by how the upward propagating waves interfered with the climatological background waves. One region that appears to be favorable for positive interference and therefore increased transfer of momentum into the stratosphere is the Barents Sea [*Kim et al.*, 2014]. *Pedersen et al.* [2015] modeled the atmospheric response to different regional changes in Arctic sea ice cover and found that the midlatitude response is sensitive to where the sea ice anomalies are located. In particular, the position of the northern center of the North Atlantic Oscillation pattern was found to be sensitive to the location of the sea ice reductions. *Koenigk et al.* [2016] investigated the seasonal prediction skill of winter climate conditions in the northern midlatitude and high latitude, using sea ice area in different Arctic subregions as predictors. They found that November sea ice variations in the Barents and Greenland Seas play an important role for the sign of the wintertime North Atlantic Oscillation, whereas the amplitude and spatial extent of the teleconnection pattern can be modulated by sea ice variations in the Labrador Sea.

Despite the potential importance of regional sea ice changes, the most common metric to quantify Arctic sea ice variability and trend is the total Arctic sea ice extent (SIE). (SIE is defined as the area of grid boxes covered by at least 15% sea ice in a specified region.) The total Arctic SIE may, however, fail to capture many important aspects of Arctic sea ice variability; for example, transport of sea ice from one region to another could cause important regional anomalies with no change in the total sea ice cover. Some studies have investigated the sea ice variability and trends in specific regions [e.g., *Cavalieri and Parkinson*, 2012], but these regions are usually defined based on geography rather than the dynamic and thermodynamic characteristics of sea ice, so these regional sea ice quantifications may also fail to capture the most important features of the system.

Another common issue with the quantification of sea ice changes is how to define the long-term trend. Observational studies that investigate relations between variables often detrend time series prior to analysis to avoid spurious correlations due to a common trend. The most frequently used method to identify trends is linear fitting to time series. However, the accelerating decline of Arctic sea ice makes a linear trend a poor fit, especially in the most recent years, when the linear trend would severely underestimate the rapid decline in SIE. For this reason some studies employ a polynomial fitting instead [e.g., *Tang et al.*, 2013], but this method has no physical basis and is strongly dependent on a priori assumptions about the shape of the time series. Furthermore, such trends are likely to be sensitive to the addition of new data points.

In this study we ask (1) which regions in the Arctic exhibit similar interannual variability in sea ice concentration (SIC; a measure of the area fraction covered by sea ice in a grid box), (2) what are the characteristics of regional sea ice extent (RSIE) changes in these regions and how are they related to each other, and (3) are the RSIEs variations associated with different winter weather patterns than the total Arctic SIE variations? We used SIC data obtained from satellite passive microwave observations over the 1979–2014 period to classify the Arctic sea ice cover into different subregions in autumn and early winter. Grid points with similar interannual SIC variability were objectively classified as one sea ice region using an artificial neural network technique called self-organizing map (SOM). This kind of classification is similar to other climate classifications such as the well-known Köppen climate classification, which has proven useful and successful for quantifying climate variability and change [e.g., *Chan and Wu*, 2015; *Chen and Chen*, 2013]. To detrend the time series, we used an adaptive technique known as Ensemble Empirical Mode Decomposition (EEMD). The EEMD method makes no a priori assumptions about the shape of the data and works well with nonlinear and nonstationary time series, allowing fits to the nonlinear trends in Arctic sea ice while avoiding the strong sensitivity of, e.g., polynomial fits. Based on the sea ice region classification, we assessed the regional variability and trends in RSIEs and quantified the correlation of interannual RSIE variability between different regions and seasons. Finally, to address the last question about how the RSIE variations are associated with winter weather patterns, we linearly regressed 2 m temperature and sea level pressure (SLP) onto the detrended autumn and early winter RSIEs in different regions and compared the regression patterns to the regressions onto the total Arctic SIE anomalies. In conjunction with previous studies that have found evidence that a reduction in the total summer Arctic SIE may affect the atmosphere well into the winter season [e.g., *Francis et al.*, 2009], our regression

analysis using regional Arctic sea ice anomalies can shed some light on the importance of spatial variations in the Arctic sea ice cover for the northern midlatitude and high-latitude winter weather conditions.

2. Methods

2.1. Sea Ice and Atmospheric Data

This study used SICs derived from passive microwave data from Nimbus-7 Scanning Multichannel Microwave Radiometer (SMMR), the Defense Meteorological Satellite Program (DMSP) F8, F11, and F13 Special Sensor Microwave Imagers (SSM/Is), and the DMSP F17 Special Sensor Microwave Imager/Sounder (SSMIS). The SIC data set (V1.1), which was obtained from the National Snow and Ice Data Center, has been processed to provide consistent time series of SICs spanning the coverage of these different sensors [*Cavalieri et al.*, 1996]. During transition periods when there is an overlap of data from two instruments, we chose to use the observations from the newer instrument. SMMR data were acquired every other day while SSM/I and SSMIS data are available at a daily interval. All SIC observations were provided on a polar stereographic grid with a nominal horizontal resolution of 25 km.

We focus on the Arctic sea ice variability in autumn, September–October, when the anomalies are largest, and in early winter, November–December, when the remaining anomalies may have a greater effect on the winter weather patterns, over the period 1979–2014 when satellite observations are available. Note that we do not restrict attention to the area north of the Arctic Circle; for completeness, we include the whole region defined by the SSM/I polar stereographic grid for the Northern Hemisphere and refer to this as the Arctic for convenience. Daily SICs were averaged over the September–October and November–December seasons, and the subsequent detrending and classification analyses were performed on the 2 month averaged SICs.

The different instruments on board the satellites have different-sized circular sectors near the pole where data are missing due to orbit inclination, also known as pole holes. To ensure that all grid points have a similar number of SIC data points, we used the largest pole hole (i.e., the one from the SMMR sensor) for the whole time period. Grid points that are completely ice free for more than 50% of the time over the whole time period were ignored in the subsequent analyses.

Atmospheric fields were obtained from the ERA-Interim reanalysis [*Dee et al.*, 2011]. We used monthly mean 2 m air temperature and SLP on a $1° \times 1°$ latitude-longitude grid from 1979 to 2015.

2.2. Detrending Using Ensemble Empirical Mode Decomposition

For the purpose of this study, we define a trend as low-frequency variations that result in a linear tendency over the whole time period. The trends in Arctic SICs and SIEs are, however, generally not adequately described by straight lines due to the strongly nonlinear changes in Arctic sea ice cover [*Eisenman*, 2010; *Comiso*, 2011]. There is evidence that a majority of the rate of Arctic SIE decline is externally forced [*Stroeve et al.*, 2012b], and because of the thinning of sea ice and feedback mechanisms in the Arctic climate system, it is expected that the externally forced response in Arctic sea ice cover will exhibit increasing nonlinearity [*Stroeve et al.*, 2012a]. To account for this nonlinearity and nonstationarity, we chose to detrend the sea ice data using intrinsic mode functions (IMFs) obtained from EEMD analyses [*Wu and Huang*, 2009].

Empirical Mode Decomposition (EMD), which is the basis of the EEMD technique, is an adaptive method to decompose a signal into different modes of varying frequency, called IMFs [*Huang et al.*, 1998; *Huang and Wu*, 2008]. The original signal can be reconstructed by summing all IMFs. Unlike the more traditional Fourier transform and Wavelet transform, EMD does not assume any a priori shape for the basis functions; thus, the EMD method works well for nonstationary and nonlinear data. The IMFs are instead found empirically through an iterative process that is described below.

The process to identify the IMFs through EMD is called sifting. In the first step, all extrema in the data are identified. The upper and lower envelopes that enclose all data points are defined by connecting the maxima and minima, respectively, with natural cubic spline lines. The mean of the two envelopes is then subtracted from the data. This process is repeated until the residual satisfies the criteria for an IMF: first, the number of extrema and the number of zero crossings can differ at most by one, i.e., the function should describe a function oscillating around zero; second, the mean of the upper and lower envelopes (defined by the local maxima and minima, respectively) must equal zero.

After finding the first IMF, which contains information about the highest frequency mode, the IMF is subtracted from the original data and the sifting steps are repeated to find the next IMF. Note that while the IMFs

tend to be ordered from higher to lower frequencies, the frequency of an IMF is not necessarily (and often not) constant in time. This whole process is repeated until the data have been decomposed into an appropriate number of IMFs.

EEMD is an extension of the EMD method that uses a Monte Carlo approach to obtain more robust results [*Wu and Huang*, 2009]. Because the EMD method relies on the extrema, it can be very sensitive to noise in the data. EEMD attempts to address this problem by deliberately adding white noise to the original sequence and performing EMD on an ensemble of randomly perturbed sequences. The ensemble mean of the IMFs, in which the noise ideally cancels out, is then treated as the true signal. EEMD has been shown to yield more robust results in the presence of uncertainties in the original data. In our study we used an ensemble of 100 members for the EEMD analysis and added noise with an amplitude corresponding to 0.2 standard deviations of the original data.

To detrend the SIC, SIE, and RSIE time series using EEMD, we iteratively subtracted the next lowest frequency IMF from the data until there was no detectable significant linear trend ($p \geq 0.05$). Typically, one or two IMFs were needed to detrend the time series.

2.3. Classification of Sea Ice Regions

In this study we classified the Arctic sea ice cover in two seasons, autumn and early winter, for the time period 1979–2014. The detrended seasonal average SIC time series for September–October and November–December were used in the classification. We used the detrended SIC anomalies rather than the actual SICs to focus on regions with similar interannual variability of SIC. A classification on the actual SICs using our method would mostly highlight regions of large sea ice loss in recent decades.

The sea ice classifications were performed using an objective method called SOM [*Kohonen*, 1982]. A SOM is a type of artificial neural network that is commonly used to reduce high-dimensional data into a few clusters. The name refers to the fact that the SOM is trained through unsupervised learning (*self-organizing*) and that it consists of a *map* of clusters, also called nodes or neurons, which are connected to each other through a neighborhood function. It is common to arrange the nodes in a one- or two-dimensional lattice to create a map that is easy to visualize, but in principle any arbitrary map structure can be used. Nodes that are located closer to each other in the map are typically more similar, whereas nodes far apart tend to be dissimilar or of opposite sign.

The SOM algorithm consists of two phases, training and mapping. During the training phase the map of nodes is initialized (often using the first two principal eigenvectors of the input data) and trained using competitive learning, either sequentially or, as was done in this study, through a batch algorithm. After the map has been trained, data points can be mapped to the nodes by calculating the Euclidean distance between the input data and each node in the map. The node with the closest distance is considered the winning node, also known as the best matching unit, and is chosen to represent the data point. This mapping reduces the input data to a smaller number of representative SOM nodes.

Each node in the map has the same dimensionality as the original data. The SOM method has been successfully applied to answer other questions about sea ice in the past, including characterizing variability of Antarctic sea ice [*Reusch and Alley*, 2007] and assessing the dependence of Arctic sea ice variability on synoptic systems [*Mills and Walsh*, 2014]. Although SOMs are usually applied to spatial fields in the geosciences [e.g., *Johnson et al.*, 2008], there is nothing that restricts the method to spatial data. Other applications of SOMs include clustering genes in the medical field, speech recognition, image searching, land cover classification, and many more [*Mwasiagi*, 2011]. We refer to *Mwasiagi* [2011] and *Johnson et al.* [2008] for more information about the SOM method.

Here we want to find which Arctic regions exhibit similar interannual SIC variability, so for our SOM analyses we used the detrended seasonal average SIC time series extracted from each grid point in the Arctic region as our training data. As a result, the nodes in our SOM will look like time series with the same number of data points as our original SIC data. After the training, we mapped the original detrended SIC time series to the SOM to classify the grid points according to the closest matching SOM node, where each node represents a sea ice region with a specific interannual SIC variability. To reduce the number of similar sea ice regions, we merged regions that share more than 50% of their variance in detrended RSIE variability. The classification was performed separately for September–October and November–December because of large differences

in the interannual sea ice variability between the two seasons, resulting in a poor training of the SOM when considered together.

The SOM analyses were carried out using rectangular lattices with 3×4 nodes for the autumn SICs and 2×3 nodes for the early winter SICs. The SOM sizes were determined based on the correlation between the SICs and the best matching units. The correlation increases as the SOM size is increased, initially fast for smaller SOM sizes, and then more slowly as the SOM size becomes larger. Our chosen SOM sizes correspond to the points at which the second derivative of the correlation versus SOM size becomes negative, i.e., when the rate of increase in correlation is decreased, which implies that the benefit from increasing the SOM size is not worth the increased number of nodes.

2.4. Sea Ice Extent and Regression Analyses

To obtain the 2 month averaged Arctic SIE and RSIEs for the different sea ice regions in September–October (autumn) and November–December (early winter), we first calculated the daily RSIEs from daily fields of non-detrended SICs and then averaged the daily RSIEs over the 2 month seasons. This procedure avoids artificial biases that can arise when calculating the RSIE using, e.g., monthly mean SICs. The RSIEs were then detrended using the same nonlinear and nonstationary EEMD detrending algorithm that was used to detrend the SICs in the SOM analyses.

We examined the atmospheric patterns in middle to late winter (January through March) that are associated with the autumn and early winter RSIE variability in the different sea ice regions by performing lagged linear regressions of seasonal and monthly mean 2 m temperature and SLP anomalies on the detrended, sign-reversed, and standardized RSIEs. The 2 m temperature and SLP anomalies were obtained by linearly detrending the time series. (We also detrended the atmospheric fields using our nonlinear EEMD detrending method but chose to present the results from the simpler linear detrending because of the negligible differences in results between the two methods.) The signs of the standardized SIE and RSIE time series were reversed to show the 2 m temperature and SLP anomalies associated with one negative standard deviation of the SIEs and RSIEs.

3. Results

3.1. Classified Arctic Sea Ice Regions

The whole extended Arctic was classified in our study into several subregions based on the interannual SIC variability in each grid point, using a SOM of 3×4 nodes in autumn (September–October) and 2×3 nodes in early winter (November–December). Throughout the rest of the paper we will refer to these Arctic subregions as sea ice regions or just regions for simplicity.

Figure 1 shows the 12 SOM nodes for the autumn season. The SOM nodes generally represent the variability of the SIC time series within each cluster well, resulting in a meaningful clustering of the data. The average correlations between the SICs and their corresponding closest SOM node (i.e., their best matching unit) in the autumn SOM range from 0.36 to 0.65. (Note that the correlations between the SOM nodes and the median SIC time series in each node are much stronger, typically above 0.7 and greater than 0.9 in four nodes.) There is one exception to this medium to strong correlation, the node on the third row and second column, which is only weakly correlated to the SICs ($r = 0.07$). The reason for this weak average correlation is due to the fact that this SOM node and the detrended SIC time series mapped to this node exhibit close to zero interannual variability; thus, even if the Euclidean distances between the node and the time series are small, the correlations between them are not necessarily high. The SOM node on the third row and second column does a good job capturing the characteristics of the clustered time series, representing grid points with a distinctively small interannual SIC variability. The average correlation between the SICs and corresponding best matching units for all nodes in autumn is 0.43. In early winter the correlations between the SICs and best matching units generally range from 0.31 to 0.60, again with a SOM node (W5) representing small interannual SIC variability that is weakly correlated to the SICs ($r = 0.17$), with an average correlation of 0.37 across all nodes.

Three adjacent SOM nodes in autumn representing the SIC variability in the Laptev-East Siberian Seas were sufficiently similar (i.e., greater than 50% shared variance) that it proved convenient to merge them for interpretations. Similarly, we combined two adjacent nodes representing the SIC variability in the Barents-Kara Seas into one sea ice region. The total number of autumn sea ice regions was thereby reduced from the 12 SOM nodes to 9 merged sea ice regions. There were no such strong correlations between the six early winter SOM nodes, so we ended up with six sea ice regions in early winter, one for each node.

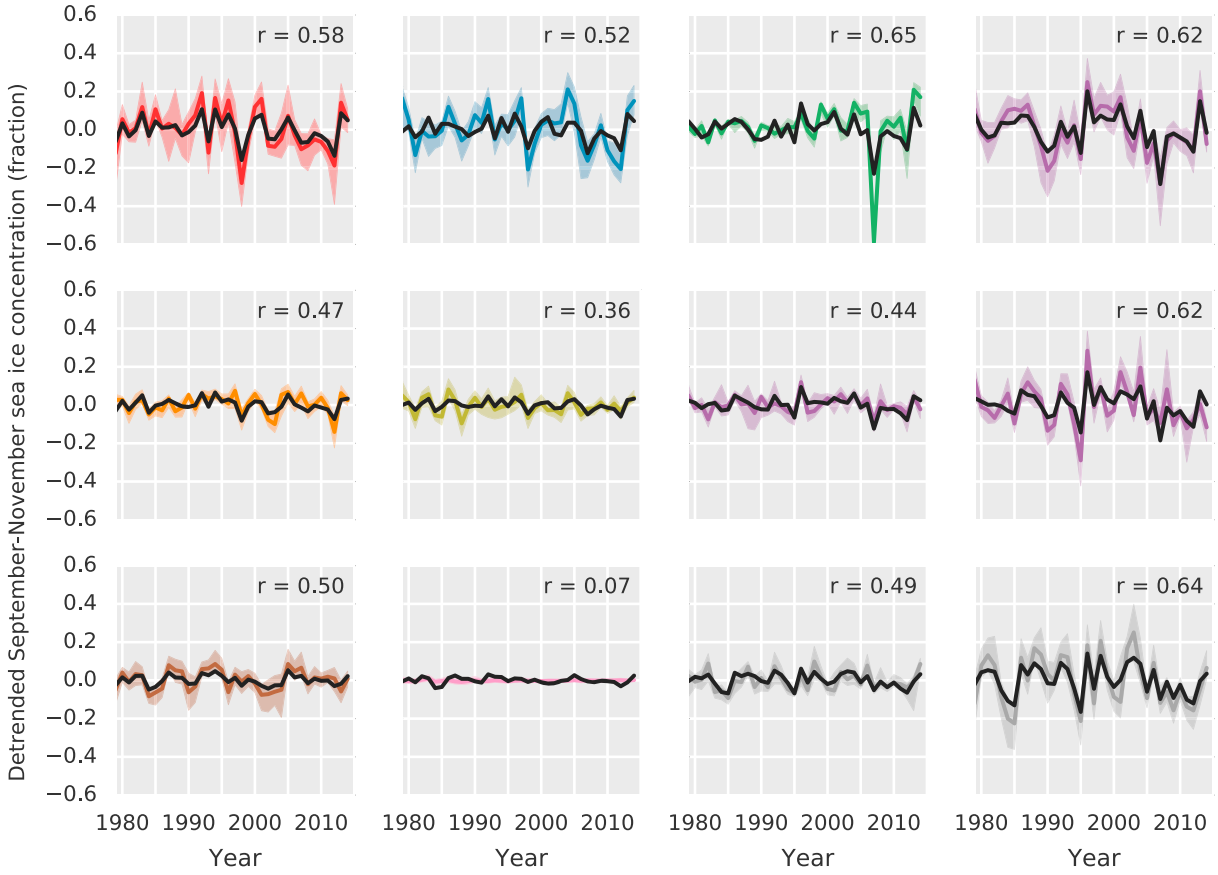

Figure 1. Map of the SOM nodes for the autumn (September–October) season and corresponding SIC time series. Black lines show the SOM nodes, colored lines show the median of all SIC time series that belong to each node, and colored shadings show the range from the lower quartile to the upper quartile of the classified SIC time series. The colors correspond to the color of the sea ice regions in Figure 2a. The numbers in the upper right corner of the nodes indicate the average correlation between the node and the SIC time series that belong to that node.

The autumn and early winter sea ice regions are shown in Figure 2. As one might expect, we find that grid points with similar SIC variability tend to be located geographically close to each other, forming larger and often contiguous subregions within the Arctic region. For convenience of discussion we numbered the sea ice regions, starting from the upper left nodes and going across and then down the SOM lattices, and prefixed the numbers with the letter "A" for the autumn regions and "W" for the early winter regions. To ease the comparison of the autumn and early winter regions, we renumbered and recolored the early winter regions based on the temporal RSIE correlation and geographical closeness to the autumn regions. Specifically, we reordered the early winter regions to maximize the average correlation of detrended RSIEs between the autumn and early winter regions that share the same color in Figure 2. We deliberately chose to not make the numbers between the autumn and early winter regions match to emphasize that the autumn and early winter regions are not identical. Although there is a general agreement between the regions in the two seasons in terms of geographical location and RSIE variability, there are also regions in early winter that do not correspond well to any autumn regions.

In autumn (Figure 2a) we identify four major sea ice regions, in the vicinity of the Beaufort Sea (A1), the Laptev-East Siberian Seas (A4), the Greenland Sea (A7), and the Barents-Kara Seas (A9). These sea ice regions correspond to the four corner nodes of the SOM lattice, i.e., the nodes in the SOM with most dissimilar SIC variability. There are two regions of medium size, A3 located northward of the Laptev-East Siberian Seas and the western Beaufort Sea, and A8 to the north and west of the Queen Elizabeth Islands and along the coasts of the continents. Finally, we find three smaller and more discontinuous regions close to the Canadian Arctic Archipelago (A2, A5, and A6).

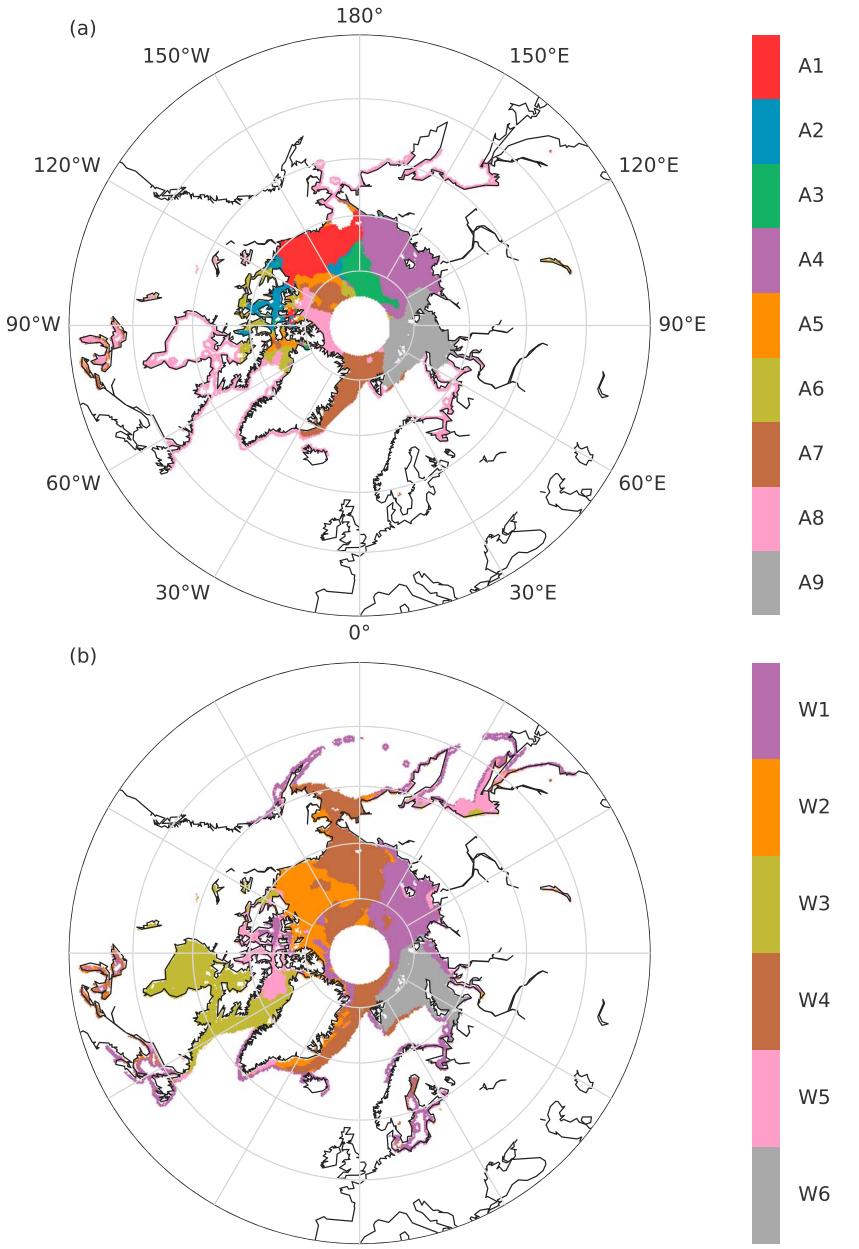

Figure 2. Regions of similar interannual Arctic SIC variability in (a) autumn (September–October) and (b) early winter (November–December), based on satellite data over 1979–2014. The two seasons were classified independently through SOM analyses. The colors in Figure 2b were chosen to make it easier to compare the two maps, but note that regions that share the same color between the two seasons do not necessarily correspond well to each other.

Figure 2b shows the corresponding classification for the Arctic SIC during early winter. This season has five major sea ice regions, in the Laptev-East Siberian Seas (W1), the Beaufort Sea (W2), Hudson Bay extending up to southern Baffin Bay (W3), the Greenland Sea, the northern Bering Sea and the Chukchi Sea (W4), and the Barents-Kara Seas (W6). Grid points classified as W5 are mostly found around the Canadian Arctic Archipelago and the Sea of Okhotsk. A summary of the geographical locations of the sea ice regions in autumn and early winter can be found in Table 1.

We tested the robustness of our Arctic sea ice classifications by adding random white noise to the detrended SIC time series at each grid point and then repeating the SOM training and mapping. With a noise amplitude of 0.2 standard deviations of the original data, the classifications using the perturbed SICs produced similar results to the classifications shown in Figure 2, with more than 94% of the grid points matching the original

Table 1. Approximate Correspondence Between Sea Ice Regions and Geographical Locations

Sea Ice Region	Geographical Locations
	Autumn
A1	Beaufort Sea
A2	Along the Canadian Arctic Archipelago and north of the Beaufort Sea
A3	North of the East Siberian Sea and Chukchi Sea
A4	East Siberian Sea and Laptev Sea
A5	North of the Beaufort Sea
A6	Baffin Bay and along the coast of the Nunavut mainland
A7	Denmark Strait, Greenland Sea, Fram Strait, and north of the Beaufort Sea
A8	North of the Greenland and the Queen Elizabeth Islands, and along the coasts of the continents
A9	Barents Sea and Kara Sea
	Early Winter
W1	East Siberian Sea and Laptev Sea
W2	Beaufort Sea, Denmark Strait, and Greenland Sea
W3	Baffin Bay, Davis Strait, Labrador Sea, and Hudson Bay
W4	Denmark Strait, Greenland Sea, Fram Strait, Chukchi Sea, and Bering Sea
W5	Sea of Okhotsk, Baffin Bay, and along the Canadian Arctic Archipelago
W6	Barents Sea and Kara Sea

classification in both seasons (averaged result over 10 repetitions). Most of the discrepancies between the original classification and the classifications with perturbed SIC anomalies are found in the boundaries between the sea ice regions. When the noise amplitude was increased to 0.5 standard deviations the percentage of matching grid points decreased to 86% for the autumn season and 83% for the early winter season. One region that was found to be relatively sensitive in the tests with large perturbations was the northern Bering Sea and Chukchi Sea in early winter, where some of the grid points could be classified as either W4 or W2. On the whole, the sensitivity tests show that the sea ice classifications presented here are robust in the presence of random errors that are comparable to the observation uncertainties.

3.2. Regional Sea Ice Extent Trend and Variability in the Arctic

The average RSIEs in each sea ice region are shown in Figures 3 and 4 for the autumn and early winter season, respectively, with the total Arctic SIEs plotted in Figures 3a and 4a. We find the largest negative linear trend in RSIE during autumn in the A1 region (the Beaufort Sea), closely followed by A9 (the Barents-Kara Seas) and A4 (the Laptev-East Siberian Seas), all around −20% per decade relative to their average RSIEs over the whole time period. The linear trends in RSIE decrease in these regions are substantially larger than the negative trend in the total SIE over the whole Arctic region during the same months (−12.5% per decade). It is also apparent that the decrease in autumn RSIE has accelerated in most regions, yielding the accelerating decline in the total autumn Arctic SIE that has been noted by previous studies [e.g., *Comiso et al.*, 2008]. This accelerating negative trend in RSIE is well captured by the nonlinear trends obtained from the EEMD analysis, shown as dashed black lines in Figure 3. Overall, the RSIE trends differ between sea ice regions in autumn, and different regions exhibit distinct features of interannual RSIE variability.

Our RSIE analysis reveals that the anomalously low total Arctic SIE in 2007 was caused by a combination of a steady negative trend of RSIEs in most regions in the recent decade, plus a large loss of sea ice mainly in the A1, A2, A3, and A4 regions in 2007, all located around the Laptev-East Siberian Seas and the Beaufort Sea. A3 north of the northern Laptev-East Siberian Seas, in particular, shows a relatively steady RSIE of approximately 0.6 million km^2 until 2007, when it abruptly dropped to less than one third of its original value. After 2007, the RSIE in A3 exhibits a more prominent year-to-year variability that is similar to the changes in the total SIE, likely due to some thinner first-year sea ice replacing multiyear ice in this region. The record-low Arctic SIE observed in 2012 was associated with anomalously low RSIE in multiple sea ice regions, including A1, A2, A3, A4, and A5 (located around the Laptev-East Siberian Seas and the Beaufort Sea), A9 (the Barents-Kara Seas), and to some extent A6 (around Baffin Bay).

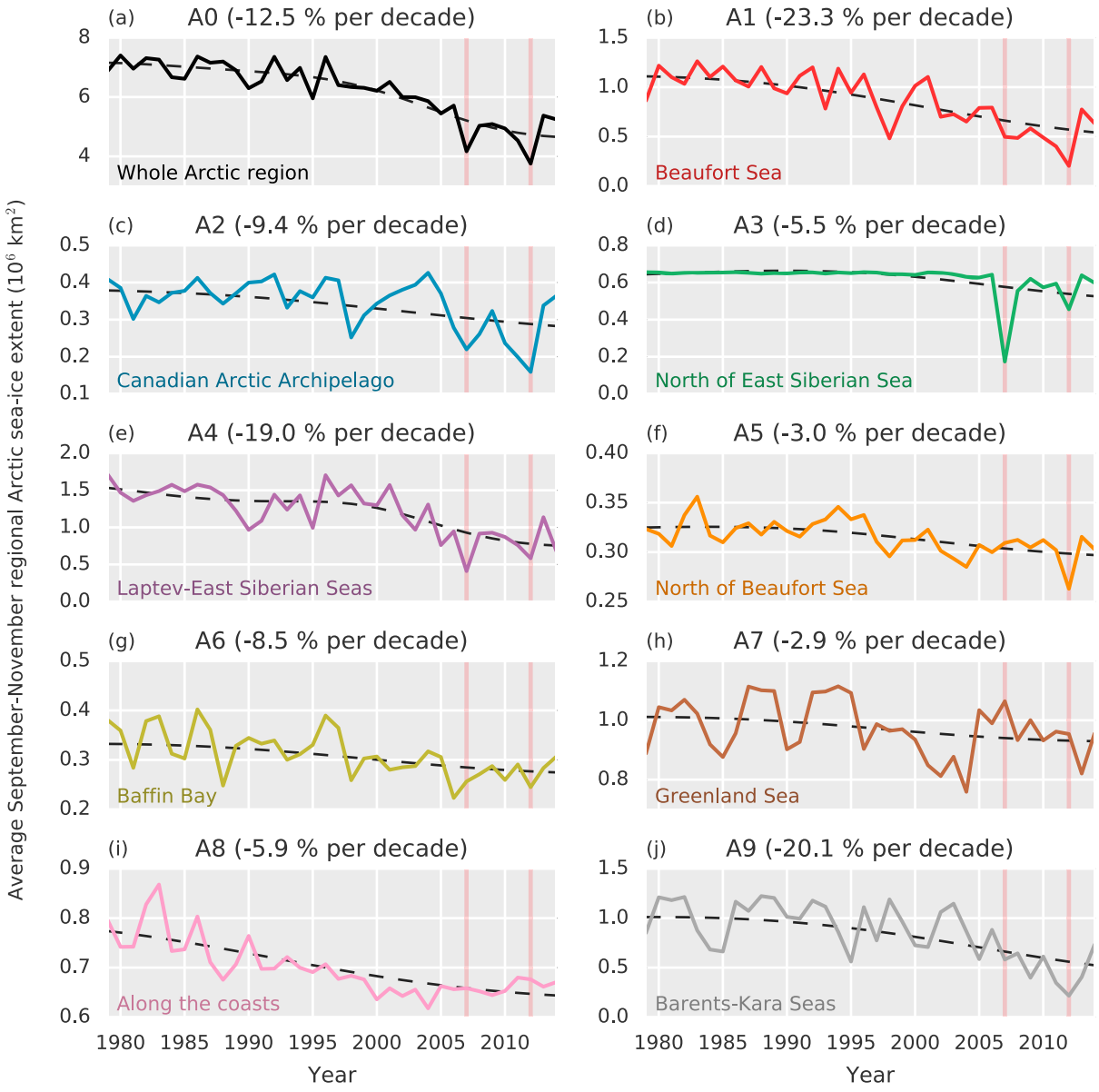

Figure 3. Time series of average Arctic SIE and RSIEs during autumn (September–October) in (a) the whole north polar region and (b–j) the sea ice regions depicted in Figure 2a. Black dashed lines show the nonlinear and nonstationary trends obtained using the EEMD method. Red vertical lines mark 2 years of exceptionally low total Arctic SIE (2007 and 2012). The numbers within parentheses in the titles show the linear trend in SIE/RSIE in a particular region relative to the 1979–2014 average SIE/RSIE in that region.

Figure 4 shows the time series of SIE and RSIEs in the early winter sea ice regions. Note that the RSIEs in 1987 were omitted because of a large amount of missing satellite data in December that year. The largest linear decline in early winter RSIE is found in the W3 region around Hudson Bay (−12.4% per decade) followed by W6 in the Barents-Kara Seas (−10.7% per decade). The magnitudes of the linear trends in these regions are about 2–3 times larger than the linear trend in the total early winter Arctic SIE (−4.1% per decade). Compared with W3 and W6, the other sea ice regions show considerably smaller linear trends in sea ice loss. The nonlinear trends from the EEMD analysis show that the total Arctic SIE in early winter remained relatively stable prior to 1990, decreased with an accelerating negative trend in the late 20th and early 21st century and slowed down its decline in the last decade, largely due to the large recovery of SIE in 2013 and 2014. The Laptev-East Siberian Seas (W1) and the Barents-Kara Seas (W6) still exhibit an accelerating negative trend in their RSIEs at the end of the time series. The other sea ice regions show negative but decelerating nonlinear trends.

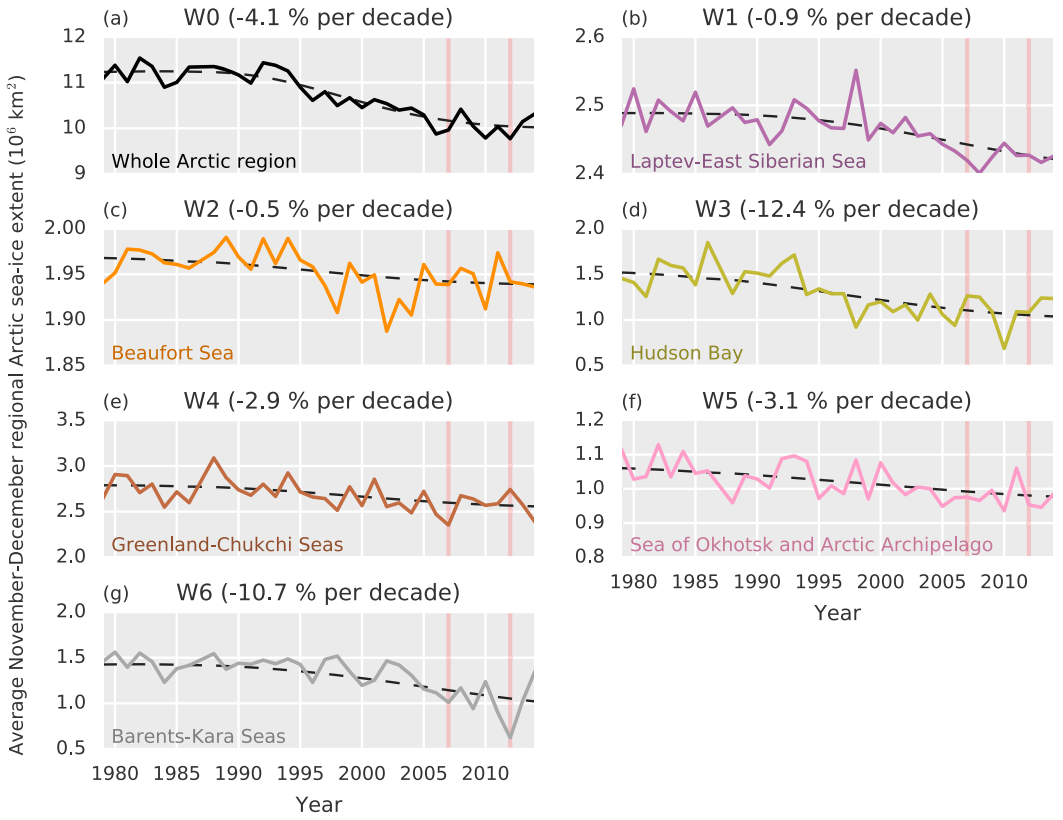

Figure 4. Time series of average Arctic SIE and RSIEs early winter (November–December) in (a) the whole north polar region and (b–g) the sea ice regions depicted in Figure 2b. Black dashed lines show the nonlinear and nonstationary trends obtained using the EEMD method. Red vertical lines mark 2 years of exceptionally low total Arctic SIE (2007 and 2012). The numbers within parentheses in the titles show the linear trend in SIE/RSIE in a particular region relative to the 1979–2014 average SIE/RSIE in that region.

All regions show a recovery of sea ice in the most recent year (2014) except for W4 (the Greenland-Bering-Chukchi Seas), where 2014 had the second lowest RSIE on record, comparable only to the record-low RSIE in 2007. Overall, the trends in Arctic RSIEs are all negative in both seasons and differ only in magnitude.

In Figures 5 and 6 we subtracted the nonlinear EEMD trends from the RSIEs in September–October and November–December, respectively, to focus on the interannual variability of the total Arctic SIE and RSIEs. The SIE and RSIEs were standardized to one standard deviation to facilitate comparison between different regions. Figure 5a shows that the total autumn Arctic SIEs in 2007 and 2012 were anomalously low even without the nonlinear trend. There is a strong relationship between the autumn RSIE variability in the Laptev-East Siberian Seas (A4) and the total SIE variability, with a shared variance of 44.6%. The total SIE is also well related to the RSIE variability in the Beaufort Sea (A1; 34.9% shared variance) and, somewhat surprisingly, the northern part of the Laptev-East Siberian Seas (A3; 36.1% shared variance). (Note that the shared variances add up to more than 100% because the RSIEs also share variance with each other.) A2 north of the Beaufort Sea and A9 in the Barents-Kara Seas both share about one fourth of their variance with the total SIE, while the RSIEs in the remaining regions are weakly correlated to the SIE in the whole Arctic region. The RSIE anomalies in A7 and A8 in the Greenland Sea and north of the Queen Elizabeth Islands are particularly independent of the total SIE variability (1.0% and 0.0% shared variance, respectively). A8 reflects to a large part sea ice along the coasts, and it therefore makes sense that the RSIE in this region exhibits variability that is unrelated to the total SIE in the Arctic Ocean. The RSIE in the Greenland Sea (A7) is well related to the total SIE in the first one third of the time series (correlation coefficient of about 0.7), but in the latter two thirds, especially in the most recent decade, the two time series are strongly anticorrelated (correlation coefficient of about −0.5 to −0.6), resulting in a weak correlation over the whole time period.

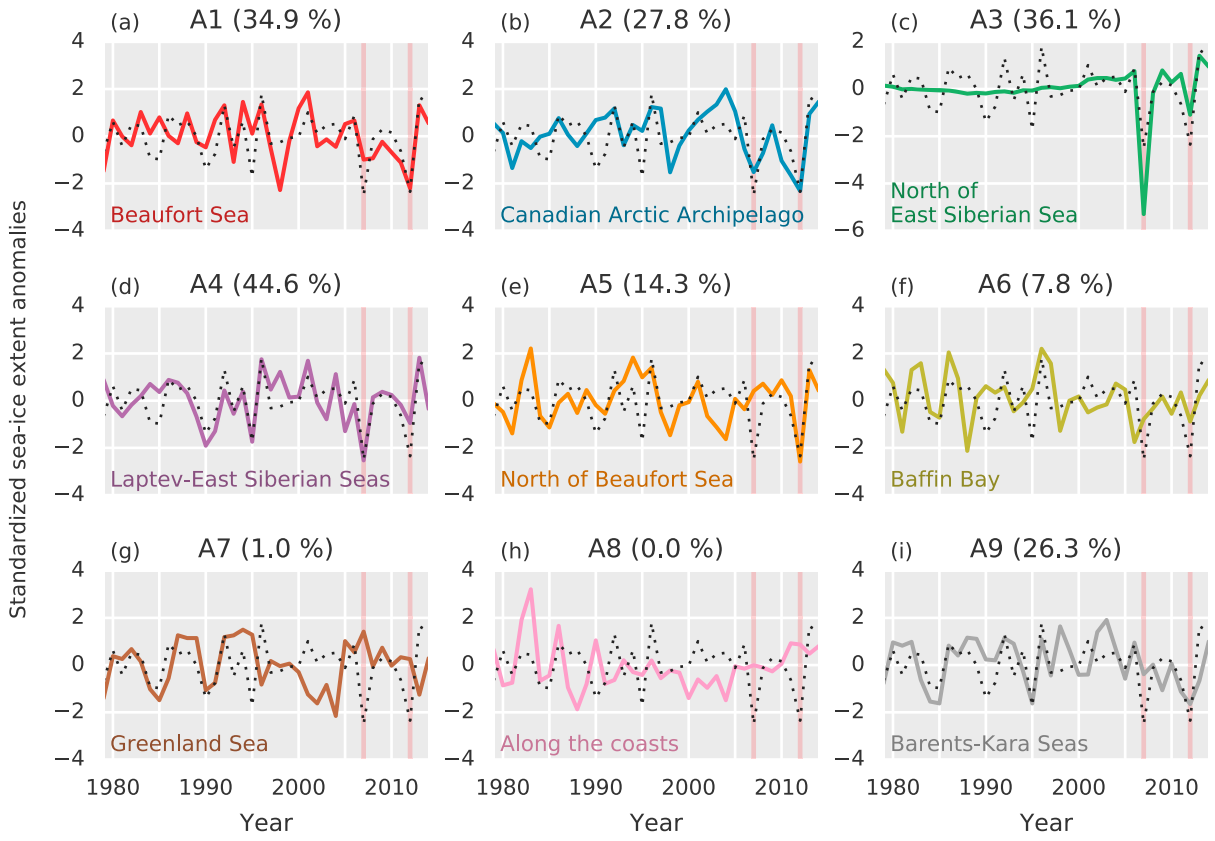

Figure 5. (a–i) Time series of regional Arctic RSIE anomalies in autumn (September–October). The anomalies were standardized to one standard deviation after subtracting the nonlinear trends from the original time series. Black dotted lines show the detrended SIE anomalies in the whole Arctic region. Red vertical lines mark 2 years of exceptionally low Arctic SIE (2007 and 2012). The numbers within parentheses in the titles show the percentage of shared variance (r^2) between the total SIE anomaly variability and the RSIE anomaly variability in a particular sea ice region.

We note that the sea ice in the Greenland Sea (A7) shows a strong multiyear variability in the first half of the time series, but in the latter half there is large interannual variability. The interannual RSIE variability in the region north of the Queen Elizabeth Islands and along the coasts (A8), on the other hand, has decreased in the recent decade compared with the relatively large variability in the beginning of the time series. The Beaufort Sea (A1) exhibits a rather regular year-to-year variation in its RSIE in the first half. In 1998 there was huge loss of sea ice in the Beaufort Sea region, and afterward the RSIE variability in the Beaufort Sea became more irregular. The RSIE in the Barents-Kara Seas (A9) has been unusually low in the recent decade even with the long-term negative trend removed, especially in 2012, although the negative RSIE anomaly in 2012 was not unprecedented, as RSIE anomalies of similar magnitudes were observed in 1984, 1985, and 1995. All sea ice regions except A4 in the Laptev-East Siberian Seas show a positive RSIE anomaly in the most recent year (2014).

Figure 5c reveals that the large RSIE decrease in 2007 in the A3 region north of the Laptev-East Siberian Seas was highly unusual, about five standard deviations below the trend line. This large RSIE anomaly clearly demonstrates the benefits of using EEMD to obtain the long-term trend. A linear fitting would be heavily skewed toward the negative anomaly in 2007, resulting in an artificially large negative trend, while a polynomial fitting would have to be carefully chosen to match the trend, and would likely not be robust to future observations. The trend line from the EEMD analysis is not as heavily influenced by the 2007 anomaly because this RSIE change occurs on a time scale shorter than the low-frequency variability that makes up the trend. Thus, the EEMD analysis considers the 2007 anomaly to be a large deviation from the trend rather than part of the long-term trend.

In early winter the total Arctic SIE is mostly controlled by two sea ice regions, W3 and W6 in Hudson Bay and the Barents-Kara Seas, respectively, sharing 27.2% and 25.6% of their variance with the total SIE (see Figure 6). The other sea ice regions in early winter share less than 10% variance with the total SIE. The W1 region in

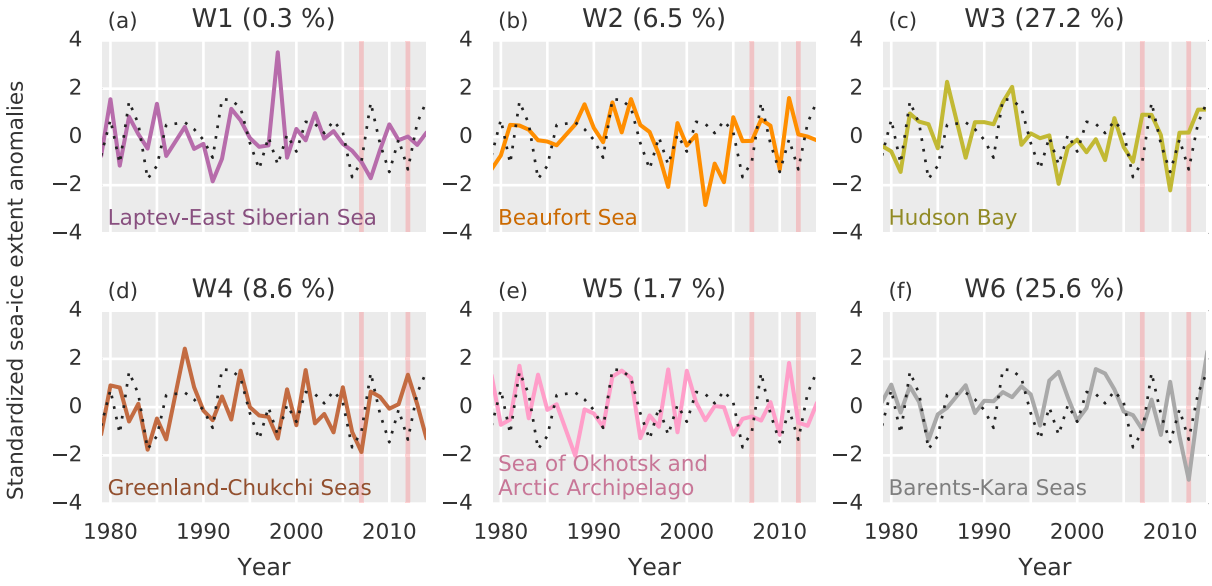

Figure 6. Time series of regional Arctic RSIE anomalies in early winter (November–December). The anomalies were standardized to one standard deviation after subtracting the nonlinear trends from the original time series. Black dotted lines show the detrended SIE anomalies in the whole Arctic region. Red vertical lines mark 2 years of exceptionally low Arctic SIE (2007 and 2012). The numbers within parentheses in the titles show the percentage of shared variance (r^2) between the total SIE anomaly variability and the RSIE anomaly variability in a particular sea ice region.

particular, located in the Laptev-East Siberian Seas just east of the W6 region, is mostly unrelated to the total SIE, with only 0.3% shared variance between the two time series. This is a striking contrast to the autumn season when the RSIE in the Laptev-East Siberian Seas (A4) is strongly related to the total SIE (44.6% shared variance). W2 in the Beaufort Sea and along the east coast of Greenland is the early winter region that exhibits the strongest decadal variability and relatively small trend. The RSIE in W2 was anomalously low for almost a decade in the late 20th century and early 21st century, while the detrended RSIE was relatively high the decade before that. In the most recent decade the RSIE in W2 has been near or slightly above the trend line. Recently, there has been a marked increase in the magnitude of RSIE variability in the Barents-Kara Seas (W6), with a large decrease in RSIE in 2012 of more than 3 standard deviations that was unprecedented in the satellite period even with the trend removed. W6 is the only early winter region that shows a clear signature of the

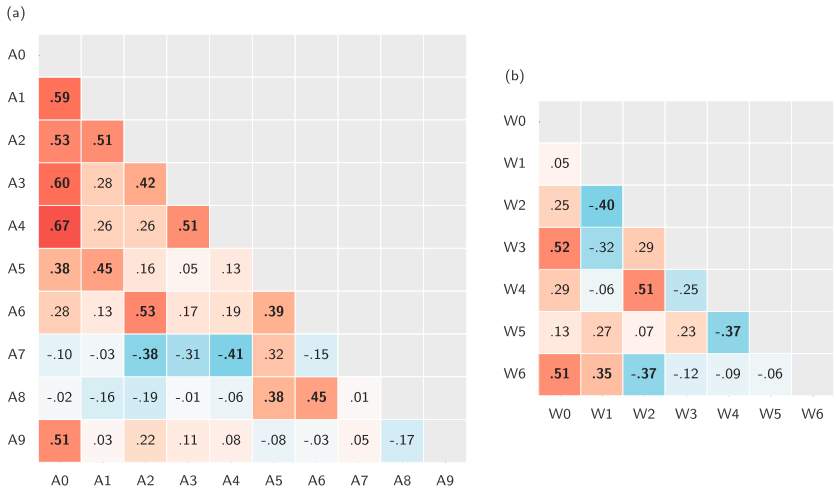

Figure 7. Correlations between detrended RSIEs in different sea ice regions during (a) autumn (September–October) and (b) early winter (November–December). A0 and W0 denote the total Arctic SIE anomalies in autumn and early winter, respectively. The numbers show the correlation coefficients, positive correlation coefficients are shaded red, and negative correlation coefficients are shaded blue. Bold correlation coefficients are statistically significant at the 0.05 significance level.

large loss of autumn RSIE in 2012. Indeed, although the total early winter Arctic SIE was well below the trend line in 2012, this deviation was not unusually low when considering the interannual variability of the whole time series, only slightly more than one standard deviation below the trend.

Figures 7a and 7b show the correlations of interannual RSIE variability between sea ice regions in the same season in September–October and November–December, respectively. As given above, we use A0 to denote the total Arctic SIE in the autumn season, and W0 for the total SIE in early winter. The correlation coefficients were calculated after subtracting the nonlinear trends from the SIE and RSIEs. Most sea ice regions in autumn show a positive correlation with the other regions (Figure 7a). As previously noted, the majority of the regions show a moderate to strong positive correlation with the total SIE; exceptions are the A6, A7, and A8 regions around the Canadian Arctic Archipelago, the Greenland Sea, the Queen Elizabeth Islands, and along the coasts. The correlations between RSIE anomalies in sea ice regions close to each other tend to be moderate to strong. A7 in the Greenland Sea is not strongly correlated to any other regions and is the only region with significant anticorrelations in autumn, likely due to sea ice drift from the Arctic Basin to the Greenland Sea through Fram Strait. The interannual RSIE variability in the Barents-Kara Seas (A9) is mostly independent from the other sea ice regions, but it still plays a significant role for the total autumn SIE variability in the Arctic.

In early winter the correlations of RSIEs between sea ice regions are generally not as strong as in autumn and show a larger number of significant negative correlations (Figure 7b). Although the total SIE variability in early winter is mostly controlled by the RSIE variability in Hudson Bay (W3) and the Barents-Kara Seas (W6), these two regions are not well related to each other. The RSIE variability in the Barents-Kara Seas (W6) is moderately positively correlated to the RSIE in the Laptev-East Siberian Seas (W1) and weakly to moderately anticorrelated with the other regions.

The correlations between the sea ice regions in autumn and early winter are shown in Figure 8. We find weak to moderate positive correlations between RSIEs in autumn and the total SIE (W0) in winter, with statistically significant correlations between the total early winter Arctic SIE and the RSIEs in the A2 and A5 regions north of the Beaufort Sea and in the Canadian Arctic Archipelago. On the contrary, a large total SIE in autumn (A0) is not well related to large RSIEs in winter except for in the Barents-Kara Seas (W6). W2, W3, and W4 in the western Arctic show moderate to strong positive correlations with autumn RSIEs in similar locations to the winter regions. The early winter RSIE in the Barents-Kara Seas (W6) is strongly positively correlated to the autumn RSIE in the approximate same location (A9), with a shared variance of 37%, and is also well related to the autumn RSIE in the distant A2 region.

3.3. Winter Weather Patterns Associated With Regional Arctic Sea Ice Extent Variability

Finally, we investigated the question whether the RSIE variabilities are associated with different winter weather patterns than the total Arctic SIE variability. We approached this question by regressing detrended 2 m temperature and SLP anomalies onto the sign-reversed and detrended RSIEs and total Arctic SIE. It is important to emphasize that our regression analyses reveal only statistical relationships, and although the regressions are lagged, correlations do not imply causation. Nevertheless, the regressions onto the RSIEs may explain some of the atmospheric variability associated with the total Arctic SIE and could point out Arctic regions where the autumn and early winter sea ice variabilities are strongly correlated to the weather patterns later in winter.

Figure 9 shows maps of wintertime (January–March) averaged 2 m temperatures regressed onto the detrended and standardized autumn SIE and RSIES. Because the SIE and RSIEs in the regression analyses were sign reversed, a positive regression indicates a positive 2 m temperature anomaly occurring with a negative SIE or RSIE anomaly (the amplitude corresponds to an SIE or RSIE anomaly of one negative standard deviation). A reduced total autumn Arctic SIE is associated with cooler temperatures over the northern Eurasian continent and warmer temperatures over Greenland and the Labrador Sea. This dipole in 2 m temperatures between the midlatitude and high latitude is commonly known as the Warm Arctic-Cold Continents pattern and has previously been attributed to sea ice loss in the Arctic [e.g., *Cohen et al.*, 2013; *Overland et al.*, 2011]. However, in our analyses the continental cooling associated with the total Arctic SIE variability over the 1979–2014 period is statistically significant in only a small part of Russia. When performing the regression analysis without detrending the 2 m temperatures and total SIE, we find a stronger positive 2 m temperature anomaly in the Arctic and weak and mostly insignificant signals in the midlatitudes.

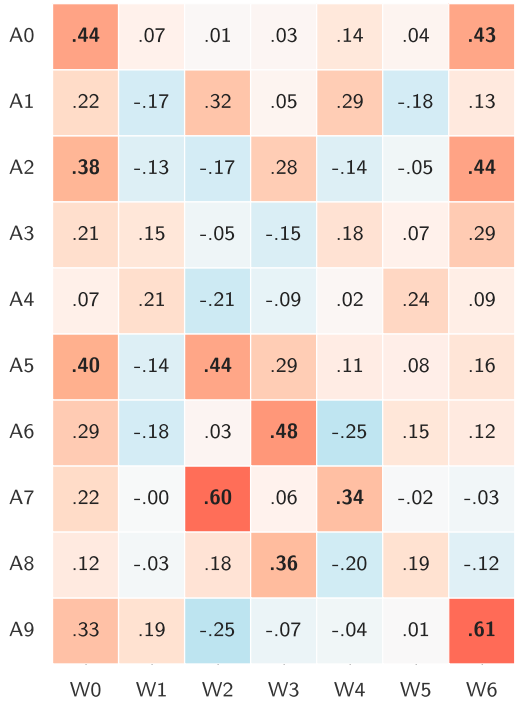

Figure 8. Correlations between detrended total and regional RSIEs in autumn (September–October) and early winter (November–December). A0 and W0 denote the total Arctic SIE anomalies in autumn and early winter, respectively. The numbers show the correlation coefficients, positive correlation coefficients are shaded red, and negative correlation coefficients are shaded blue. Bold correlation coefficients are statistically significant at the 0.05 significance level.

Looking at the 2 m temperature regression patterns in Figure 9 associated with autumn RSIEs, we find that wintertime cooling of the continents is related to anomalously low RSIE in mainly two regions, the Beaufort Sea (A1) and the Barents-Kara Seas (A9). RSIE variability in the Beaufort Sea shows a similar 2 m temperature regression pattern as the regression onto the total Arctic SIE, which is not surprising given the high correlation between the two SIEs (Figure 7a), but the cooling associated with reduced RSIE in A1 is stronger and statistically significant over most of the northern Eurasian continent. Reduced RSIE in the A9 region in the Barents-Kara Seas is associated with a wintertime warming over the Barents-Kara Seas and an even more widespread continental cooling that affects most of northern Europe and Russia. A closer examination of the regression patterns using monthly means instead of seasonal means reveals that the continental cooling associated with reduced sea ice in A1 (the Beaufort Sea) is most prominent in March, while the cooling pattern associated with A9 (the Barents-Kara Seas) is seen in January and February (not shown).

Autumn RSIE reductions in the Greenland Sea and north of the Beaufort Sea (A7 and A5) are associated with a warming over Greenland and anomalously low 2 m temperatures over northern Russia. RSIE anomalies around the Canadian Arctic Archipelago and in Baffin Bay (A2 and A6) do not show a strong relation with wintertime 2 m temperatures except for a cooling over Alaska occurring with reduced RSIEs. The significant 2 m temperature anomalies associated with reduced sea ice cover along the coasts and north of Greenland and the Queen Elizabeth Islands (A8) are also constrained to the Arctic region, with anomalously high temperatures along the coast of northern Canada and a cooling over the Barents-Kara Seas. Lastly, the 2 m temperature regression patterns onto the RSIE anomalies in A4 and A3 (the Laptev-East Siberian Seas and northward of the Laptev-East Siberian Seas) show statistically significant signals in only small regions that may arise by chance. The RSIE in A4 shares a substantial amount of variance with the total Arctic SIE (Figure 5d), and the weak correlation between the RSIE in this region and 2 m temperatures during winter could therefore mask some of the correlations that are found with the RSIEs in other regions when considering only the total Arctic SIE.

Figure 10 shows the corresponding regressions of SLP anomalies onto the autumn SIE and RSIE anomalies. A reduction in the total autumn Arctic SIE is associated with a circulation pattern that resembles the negative phase of the Arctic Oscillation, the leading mode of SLP variability in the Northern Hemisphere [*Thompson and Wallace*, 1998], with a spatial correlation of −0.79 between the regression pattern and the first

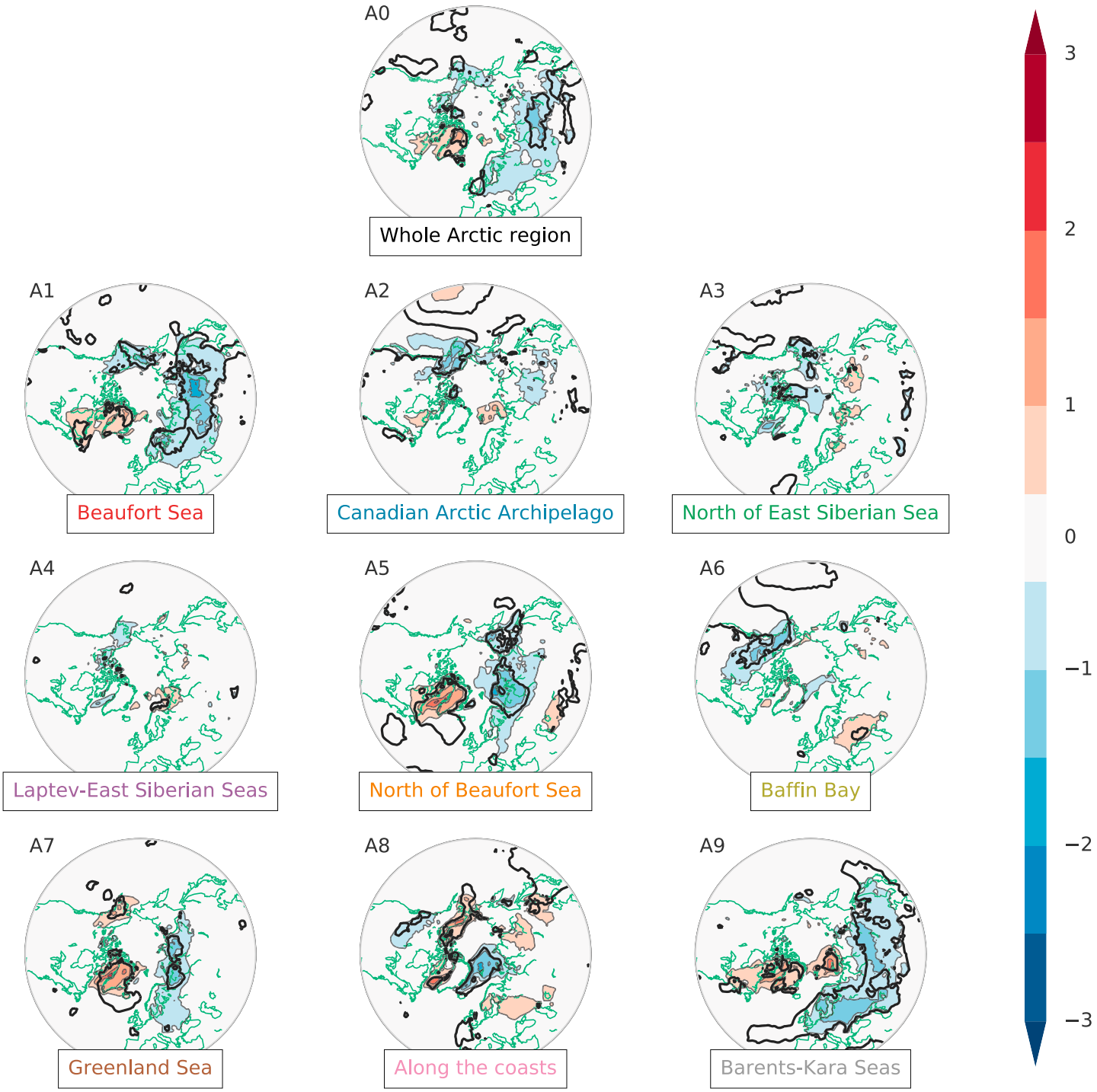

Figure 9. Linear regression of detrended average 2 m temperature in middle to late winter (January through March) onto the sign-reversed, detrended, and standardized autumn SIE anomalies in the whole Arctic region and the RSIEs in all Arctic sea ice regions. The text labels describe the approximate geographical location of the sea ice regions (see Figure 2a for more precise locations). Thick black contours indicate regions where the regression coefficients exceed the 95% significance level.

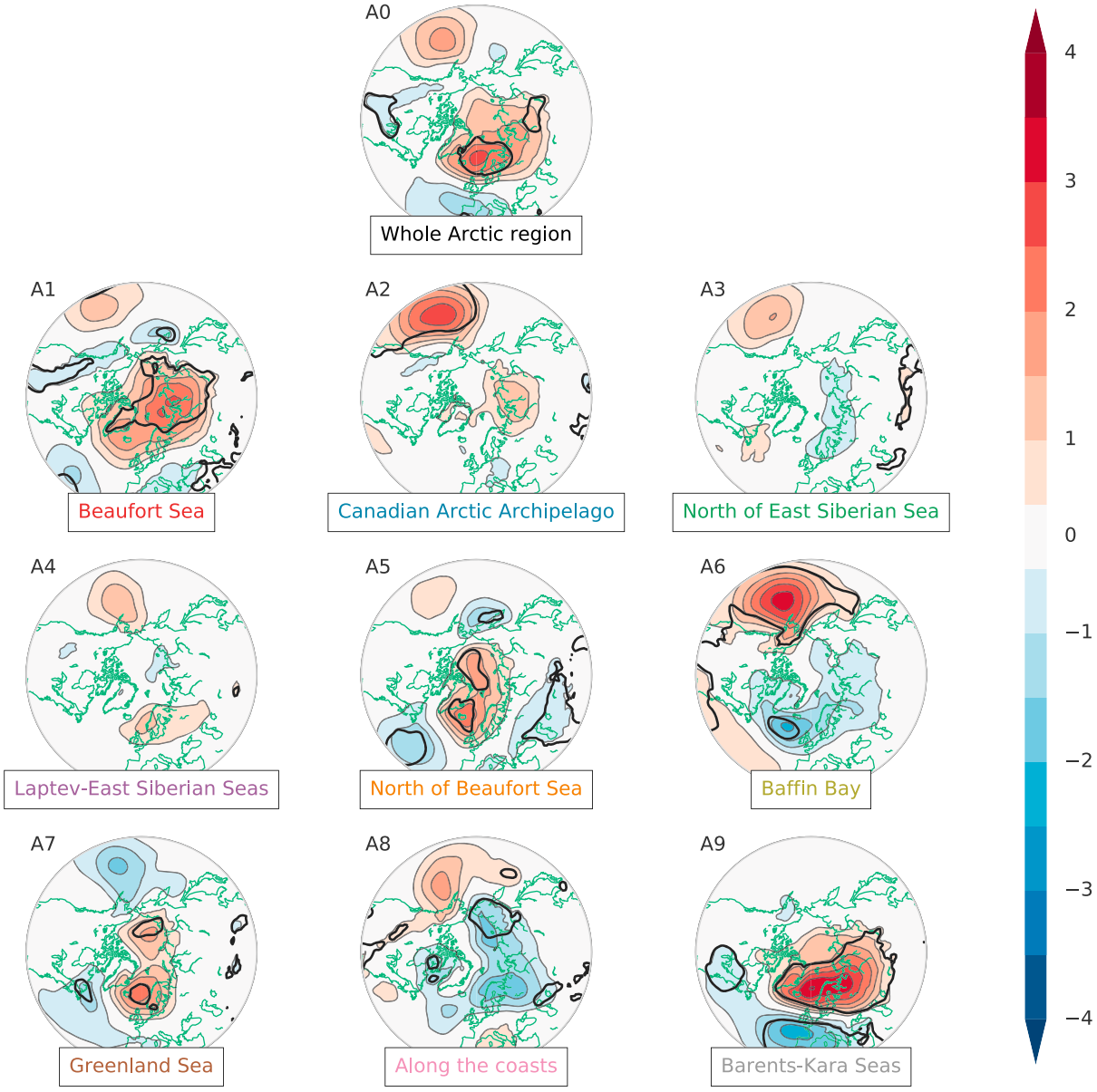

Figure 10. Linear regression of detrended average SLP in middle to late winter (January through March) onto the sign-reversed, detrended, and standardized autumn SIE anomalies in the whole Arctic region and the RSIEs in all Arctic sea ice regions. The text labels describe the approximate geographical location of the sea ice regions (see Figure 2a for more precise locations). Thick black contours indicate regions where the regression coefficients exceed the 95% significance level.

Empirical Orthogonal Function (EOF1) of wintertime SLP anomalies (the spatial fields were weighted by the square root of the cosine of latitude prior to the correlation analysis to account for the decrease in grid area with latitude). However, the regression pattern is mostly insignificant except for the positive action center over the Arctic. Negative RSIE anomalies in the Beaufort Sea (A1) are associated with a similar circulation pattern but with the positive action center over the Arctic shifted toward the Laptev Sea (spatial correlation of −0.84 with EOF1). The SLP regression pattern that most resembles the negative phase of the Arctic Oscillation is associated with reduced sea ice in the Barents-Kara Seas (A9), with a significant weakening of the Azores high and the Icelandic low, and a strong negative spatial correlation with EOF1 ($r = -0.92$). All three regression patterns have a large vertical extent stretching through the entire troposphere and a roughly equivalent barotropic structure (spatial correlation coefficients between 1000 and 300 hPa geopotential height regression patterns range from 0.69 to 0.72). These anomalous circulation patterns with higher than usual SLP over the Arctic

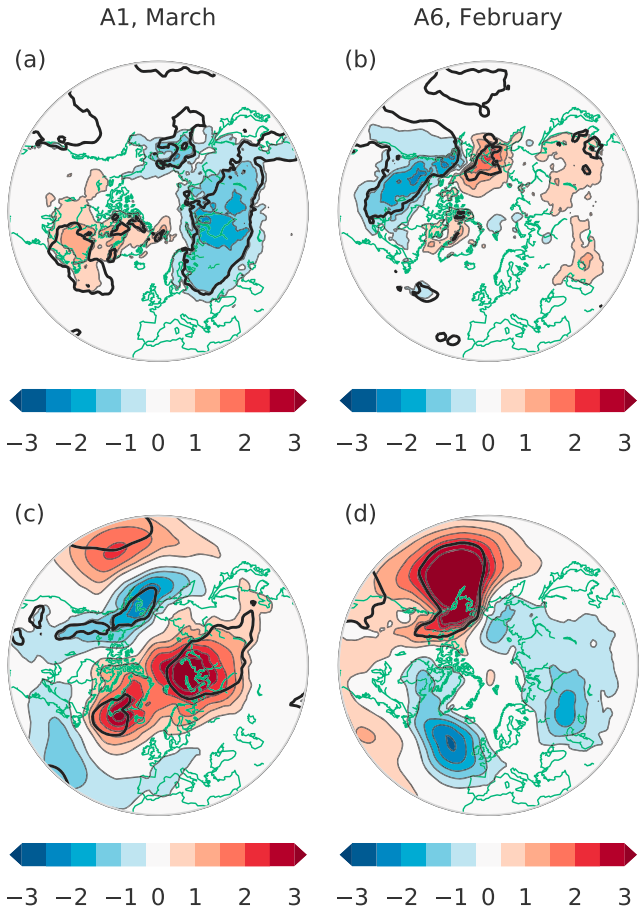

Figure 11. Linear regression of detrended monthly mean (a and b) 2 m temperature and SLP (c and d) in March (Figures 11a and 11c) and February (Figures 11b and 11d) regressed onto the regional autumn RSIE in the A1 region (the Beaufort Sea; left column) and the A6 region (Baffin Bay; right column).

could explain some of the continental cooling in Figure 9 associated with reduced sea ice in the Beaufort Sea (A1) and the Barents-Kara Seas (A9).

In the regression analyses using monthly mean SLP, the regression patterns associated with RSIE reduction in the A1 region (the Beaufort Sea) do not project strongly onto the Arctic Oscillation in any individual winter month. Instead, the A1 regression pattern in March resembles a Rossby wave train propagating over the Kara Sea, Chukchi-Bering Seas, and the North Pacific Ocean (Figure 11c). This is also the month that shows the most widespread continental cooling associated with reduced RSIE in A1 (Figure 11a). A similar wave train is identified in the composite difference of SLP fields between low and high RSIE anomaly years (below and above one standard deviation, respectively; not shown).

A significant center of positive SLP anomalies over the North Pacific Ocean is associated with decreased RSIEs in the A6 and A2 regions (in Baffin Bay and around the Canadian Arctic Archipelago). This circulation anomaly pattern is especially strong in February, with a maximum value over 4.5 hPa associated with one negative standard deviation of RSIE anomalies in A6 (Figure 11d). The resulting ridge west of North America favors increased advection of cold polar air over the North American continent, increasing the risk of unusually cold temperatures over Alaska and northwestern Canada (Figure 11b). We remark that reduced RSIEs in Baffin Bay and around the Canadian Arctic Archipelago are the only regions that show significant links with anomalously cold winters in the North American continent. Coincidental with the northwest North American cooling, there is a warming around the Chukchi-Bering Seas (Figure 11b), likely related to the anomalous southerly winds associated with the SLP pattern in Figure 11d. The SLP regression patterns associated with the RSIEs in the A6 and A2 regions project onto the second leading mode of SLP variability in the Northern Hemisphere, which is related to the Pacific/North American pattern [*Barnston and Livezey*, 1987]. The spatial correlation coefficients

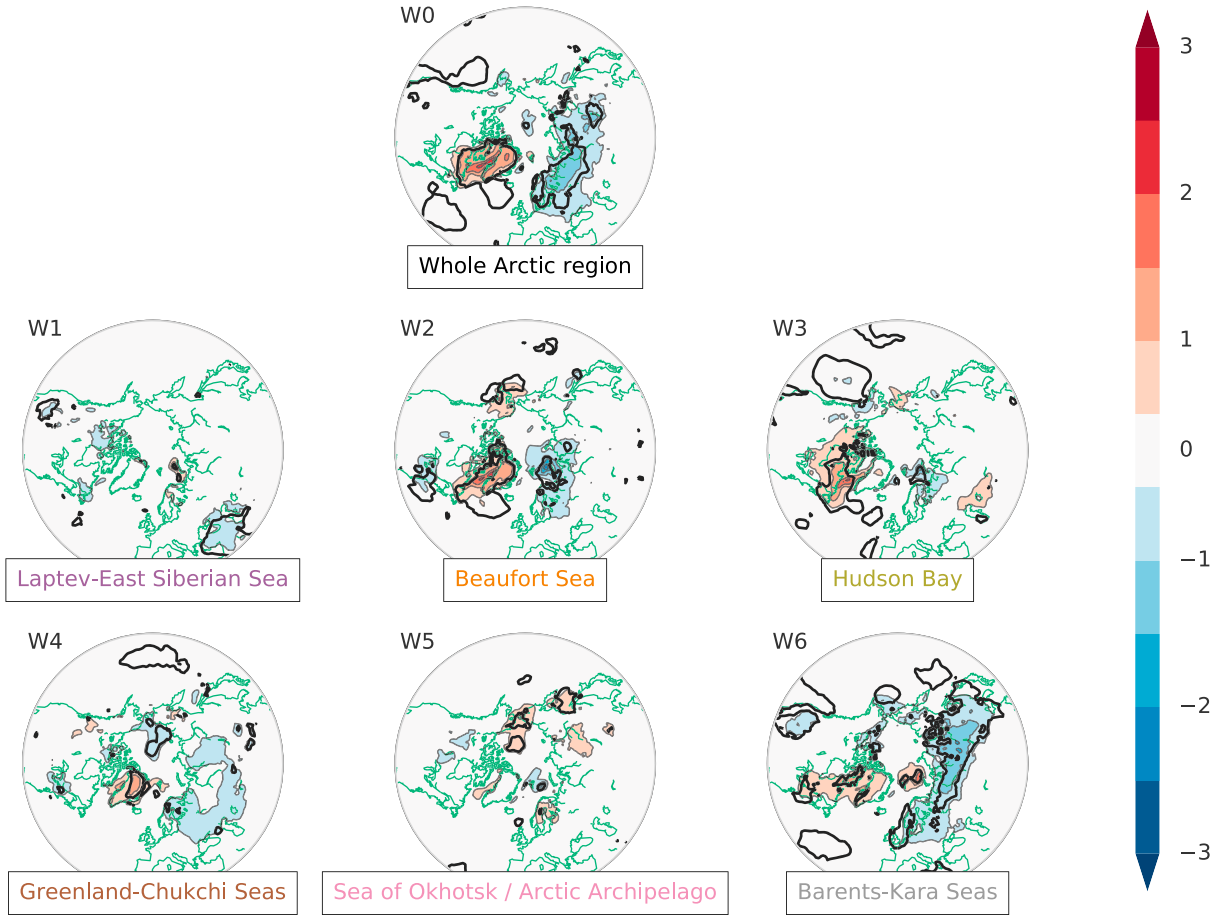

Figure 12. Linear regression of detrended average 2 m temperature in middle to late winter (January through March) onto the sign-reversed, detrended, and standardized early winter SIE anomalies in the whole Arctic region and the RSIEs in all Arctic sea ice regions. The text labels describe the approximate geographical location of the sea ice regions (see Figure 2b for more precise locations). Thick black contours indicate regions where the regression coefficients exceed the 95% significance level.

with the second Empirical Orthogonal Function are −0.82 for the A6 (Baffin Bay) region and −0.74 for the A2 (the Canadian Arctic Archipelago) region. In March the SLP regression with reduced RSIE in A6 is somewhat reminiscent of the positive phase of the AO, with a strengthening of the Icelandic low and the Azores high and a weakening of the Aleutian low, although the latter is not statistically significant.

Sea ice retreat in the Greenland Sea and north of the Beaufort Sea (A7 and A5) is associated with a weak seesaw in SLP between anomalously low pressures in the midlatitudes and anomalously high pressures in the high latitudes. These regression patterns show some similarities with the negative phase of the Arctic Oscillation (pattern correlation coefficients with EOF1 are −0.67 for A7 and −0.63 for A5). One remarkable feature of the circulation anomaly patterns associated with A7 and A5 is that they extend all the way up into the stratosphere, showing significant regression coefficients with geopotential height anomalies even at the 2 hPa pressure level. The stratospheric signal shows higher than usual geopotential heights over the Arctic and North Eurasia with reduced RSIEs in these regions, consistent with a weakening of the stratospheric polar vortex (not shown). The RSIEs in the Laptev-East Siberian Seas (A4), north of the East Siberian Sea (A3), and north of the Queen Elizabeth Islands and along the coasts (A8) do not show extensive significant regression patterns with the wintertime SLP.

Turning our attention to winter weather patterns associated with the Arctic SIE and RSIE variability in early winter, we find that reduced total Arctic SIE in early winter is related to a Warm Arctic-Cold Continents dipole in 2 m temperature between Greenland-Baffin Bay-Davis Strait-Labrador Sea and the northwestern Eurasian content (Figure 12). The anomalously high temperatures in the vicinity of Greenland associated with reduced total SIE are mostly related to regional retreat of sea ice in the Beaufort Sea (W2) and Hudson Bay

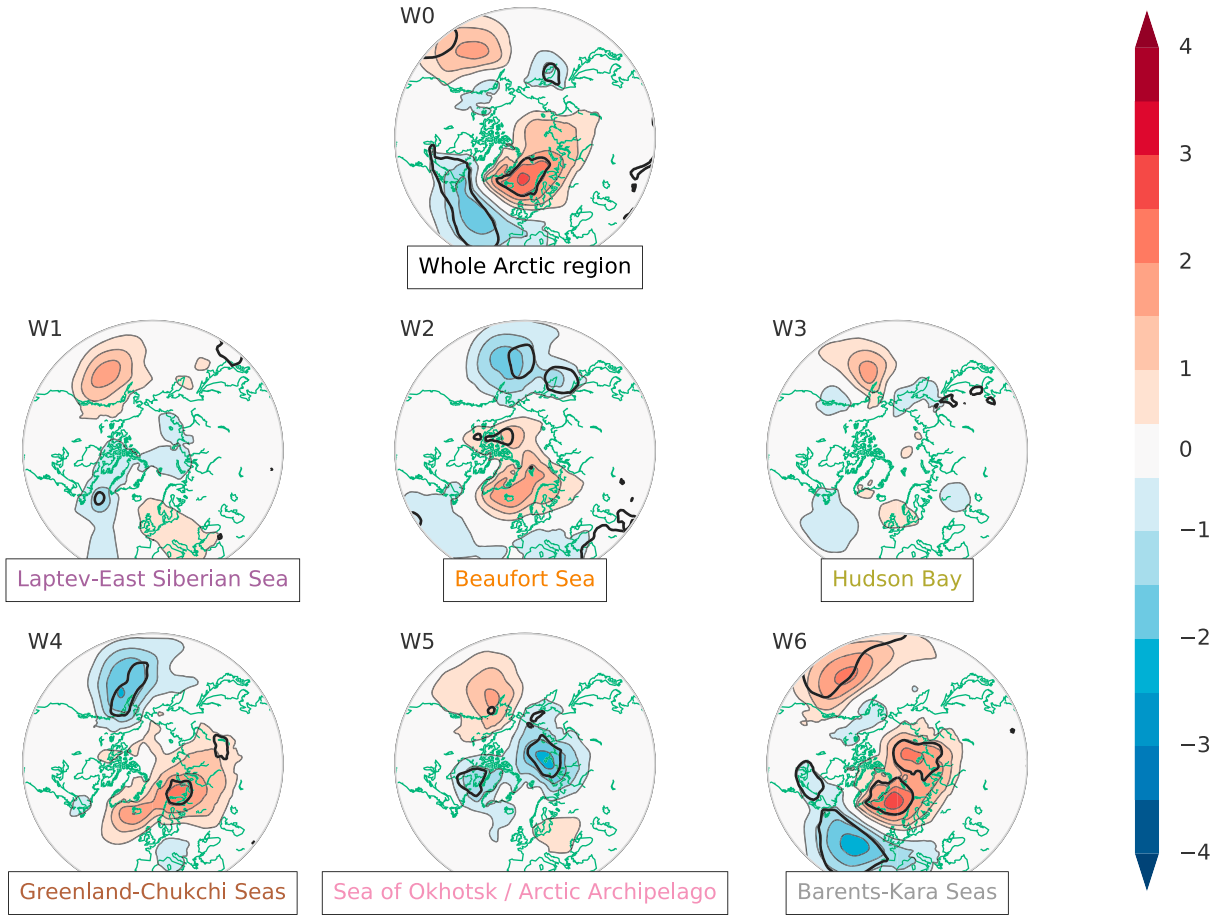

Figure 13. Linear regression of detrended average SLP in middle to late winter (January through March) onto the sign-reversed, detrended, and standardized early winter SIE anomalies in the whole Arctic region and the RSIEs in all Arctic sea ice regions. The text labels describe the approximate geographical location of the sea ice regions (see Figure 2b for more precise locations). Thick black contours indicate regions where the regression coefficients exceed the 95% significance level.

(W3), while the cold temperatures over the Eurasian content are correlated with negative RSIE anomalies in the Barents-Kara Seas (W6). The early winter RSIE variabilities in the Laptev-East Siberian Seas (W1), Greenland-Bering-Chukchi Seas (W4), and the Sea of Okhotsk and the Canadian Arctic Archipelago (W5) do not show a highly significant relationship with seasonal averaged 2 m temperature in January-March. Looking at individual months, we find that a negative early winter RSIE anomaly in the Beaufort Sea (W2) is associated with colder temperatures in Russia in March, while early winter RSIE reduction in the large Greenland-Bering-Chukchi Seas region (W4) is related to anomalously low 2 m temperatures in eastern North Europe and western Russia in February.

Figure 13 shows the SLP regression patterns associated with anomalously low early winter Arctic SIE and RSIEs. The regression onto the total early winter Arctic SIE variability shows a similar circulation anomaly to the regression onto the total autumn Arctic SIE (Figure 10). The spatial correlation between this circulation anomaly pattern associated with early winter SIE reduction and EOF1 is −0.71. Most of the association with the negative Arctic Oscillation-like pattern is related to sea ice retreat in the Barents-Kara Seas (W6), whose SLP regression pattern has a −0.66 spatial correlation with EOF1. The other regions (W1–W5) do not show more significant relations with wintertime SLP anomalies than would be expected by chance. In general, we find that the autumn RSIEs show stronger associations with the January-March circulation patterns than the early winter RSIEs.

4. Summary and Discussion

In this study we used satellite observations from Nimbus-7 and DMSP-F8, DMSP-F11, and DMSP-F17 to examine the regional changes in Arctic sea ice cover on an interannual time scale. First, we divided the Arctic sea ice cover into several smaller regions in both autumn (September–October) and early winter (November–December) through an objective self-organizing map classification based on the interannual sea ice concentration variability in each grid point. Next, we calculated the total Arctic sea ice extent (SIE) and the regional sea ice extent (RSIE) in each Arctic region and detrended the SIE and RSIEs through a nonlinear and nonstationary method known as Ensemble Empirical Mode Decomposition (EEMD). EEMD is an adaptive method that decomposes the data empirically, i.e., it does not make any a priori assumptions about the shape of the data, and captures well the strongly nonlinear trends in SIE and RSIEs. Finally, we regressed detrended 2 m temperature and SLP anomalies in winter (January–March) onto the EEMD-detrended RSIE anomalies in different sea ice regions to find out how large-scale winter weather patterns are associated with the interannual RSIE variability in each region.

We find noticeable differences in trends and variability in RSIE in different Arctic sea ice regions. The negative linear trends in RSIE are especially large in three regions during autumn, in the Beaufort Sea (A1 region), the Barents-Kara Seas (A9), and the Laptev-East Siberian Seas (A4), all three approximately −20% per decade relative to their average RSIE over the whole time period (1979–2014). During early winter the largest trends in RSIE are found in the two sea ice regions that cover Hudson Bay (W3) and the Barents-Kara Seas (W6), around −10% per decade.

Sea ice regions generally show a medium to high positive correlation in interannual autumn RSIE variability with nearby regions, and more than half of the autumn regions are strongly correlated with the total autumn Arctic SIE. One remarkable exception is the region in the Greenland Sea and north of the Beaufort Sea (A7) where the correlation between the RSIE anomalies and the total detrended autumn Arctic SIE changes sign, from a positive correlation between 1979 and around 1994 to a negative correlation from 1995 to 2013, yielding a weak correlation over the whole time period. This is also the only region where the RSIE anomalies are significantly anticorrelated with RSIE anomalies in other regions (significant negative correlations with sea ice in the Laptev-East Siberian Seas and around the Canadian Arctic Archipelago, and marginally significant negative correlations with sea ice in the region north of the Laptev-East Siberian Seas). Furthermore, the RSIE anomalies in this region show an indication of a regime shift around the same time, from dominantly multiyear (5–6 years) variability in the earlier time period to stronger interannual variability in the recent decade. We speculate that this nonstationarity of the RSIE anomaly time series in the Greenland Sea and north of the Beaufort Sea is due to a reduction of thicker multiyear ice in this region and changes in the general circulation, such as a shift in the North Atlantic Oscillation [*Hilmer and Jung*, 2000] or changes in the Arctic Dipole anomaly [*Wu et al.*, 2006], which play important roles for driving sea ice export out of the Arctic basin, through Fram Strait, and into the Greenland Sea.

The autumn RSIE in the Barents-Kara Seas (A9) varies mostly independently from the other sea ice regions but is well related to the total SIE variability. One possible reason for the lack of significant correlations in this region with other sea ice regions is that the sea ice in the Barents-Kara Seas is more strongly influenced by oceanic transport from and to the North Atlantic Ocean [*Onarheim et al.*, 2015].

Correlation coefficients between sea ice regions in early winter are generally not as strong as in autumn. The total winter SIE is significantly correlated with only the RSIE variability in Hudson Bay (W3) and the Barents-Kara Seas (W6), which is not surprising as many other parts of the Arctic are almost completely ice covered in this season or have yet to form much sea ice. There is a significant persistence of sea ice anomalies between the autumn and early winter seasons in some regions, especially in the Greenland Sea (A7 and W2) and the Barents-Kara Seas (A9 and W6).

Regressions of wintertime 2 m temperature anomalies onto the sign-reversed total autumn and early winter SIE anomalies show a dipole between warming of the Arctic and cooling of the midlatitudes associated with reduced sea ice, reminiscent of the Warm Arctic-Cold Continents pattern. However, significant regressions are rather limited in spatial extent, with most of the cooling found in northern Eurasia. Repeating the regression analysis with the RSIE anomalies resulted in stronger regression coefficients for some sea ice regions. The Warm Arctic-Cold Continents pattern is more strongly associated with autumn RSIE reduction in the Beaufort Sea (A1) and the Barents-Kara Seas (A9). There is a distinct difference in the regression patterns between these

two regions; anomalously low autumn sea ice cover in the Beaufort Sea is associated with a widespread cooling of northern Eurasia in March, while the cooling associated with sea ice loss in the Barents-Kara Seas is found in January and February. The former cooling pattern is associated with a tripole SLP pattern in March reminiscent of a Rossby wave train, whereas the SLP regression pattern associated with negative RSIE anomalies in the Barents-Kara Seas projects strongly onto the negative phase of the Arctic Oscillation.

The association between autumn sea ice reductions in the Barents-Kara and the negative phase of the wintertime Arctic Oscillation agrees well with previous observational studies [*Koenigk et al.*, 2016; *Wu and Zhang*, 2010] and modeling studies [e.g., *Pedersen et al.*, 2015; *Petoukhov and Semenov*, 2010]. Furthermore, our results of different spatial SLP patterns associated with sea ice reductions in the Barents-Kara Seas and the Beaufort Sea indicate a shift of the Arctic Oscillation toward the west and east, respectively. *Pedersen et al.* [2015] found in their model experiments that sea ice loss in the Atlantic sector of the Arctic causes a westward shift of the North Atlantic Oscillation, while sea ice loss in the Pacific sector causes an eastward shift, and this result is also consistent with the observational results of *Wu and Zhang* [2010].

Regressing the same atmospheric variables onto the early winter Arctic SIE anomalies in the whole Arctic region produced similar results as the regressions onto the total autumn Arctic SIE anomalies. Although the regions of significant regression coefficients are slightly larger in the case with the total Arctic SIE in early winter, when considering the RSIE variability in the two seasons, we find that winter weather patterns are generally more strongly associated with the RSIEs in autumn. SLP anomalies regressed onto the total early winter Arctic SIEs are mostly related to the early winter RSIE variability in the Barents-Kara Seas (W6), which is to a large part controlled by the autumn RSIE variability in the same region (37% shared variance). One reason for the weaker association with the total Arctic SIE in autumn compared with early winter is that the autumn RSIE anomalies in some regions are not well related to the winter weather patterns but still share a substantial amount of variance with the total autumn SIE, thereby masking some of the correlations with other RSIEs in the total SIE. These results highlight the potential importance of considering regional variations in Arctic SIE variability.

We stress two caveats of the regression analyses. First, the Arctic SIE and RSIEs and the atmospheric variables were detrended prior to the regressions to avoid artificial correlations due to common trends. This detrending, however, also removes some of the signals associated with Arctic amplification and the large Arctic sea ice loss in recent years. When not subtracting the trends, we generally find a more prominent warming over the Arctic and very little statistically significant cooling of the continents, as well as significant warming in the midlatitudes associated with reduced RSIE in some regions. Second, the regression patterns show only statistical links between Arctic SIE/RSIEs and atmospheric variables and do not necessarily imply a cause-and-effect relationship. Some of the regression patterns are likely not caused by the RSIE anomalies alone. The focus of this study is to diagnose and describe the RSIE variability in the Arctic, and we examined winter weather patterns associated with the RSIE variability in different regions to ascertain if the RSIEs reveal links with atmospheric patterns that are not detected when considering the total Arctic SIE. We leave the investigation of causal mechanisms behind the links between Arctic RSIE variability and winter weather patterns to future studies.

In conclusion, different regions in the Arctic exhibit distinct long-term trends and interannual variability in their RSIE. Linear regressions of 2 m temperature and SLP anomalies onto RSIEs generally result in stronger regression coefficients than when regressing the atmospheric variables onto the total SIE. We find that the regressions onto the autumn RSIE in different sea ice regions show markedly different atmospheric patterns, suggesting that regional variations in Arctic sea ice variability play an important role for the observed links with atmospheric patterns, and that some of the signals may be lost if we consider only the total Arctic SIE.

Acknowledgments
We thank the Editor, Associate Editor, and three anonymous reviewers for their helpful comments and suggestions. This research was partially supported by the E. Willard and Ruby S. Miller Faculty Fellowship. The sea ice concentration data were provided by the National Snow and Ice Data Center (https://doi.org/10.5067/8GQ8LZQVL0VL) and the atmospheric reanalysis data set by the European Centre For Medium-Range Weather Forecasts (http://apps.ecmwf.int/datasets/data/interim-full-moda/levtype=sfc/).

References

Alexander, M. A., U. S. Bhatt, J. E. Walsh, M. S. Timlin, J. S. Miller, and J. D. Scott (2004), The atmospheric response to realistic Arctic sea ice anomalies in an AGCM during winter, *J. Clim.*, *17*(5), 890–905, doi:10.1175/1520-0442(2004)017<0890:TARTRA>2.0.CO;2.

Barnes, E. A. (2013), Revisiting the evidence linking Arctic amplification to extreme weather in midlatitudes, *Geophys. Res. Lett.*, *40*, 4734–4739, doi:10.1002/grl.50880.

Barnston, A. G., and R. E. Livezey (1987), Classification, seasonality and persistence of low-frequency atmospheric circulation patterns, *Mon. Weather Rev.*, *115*(6), 1083–1126, doi:10.1175/1520-0493(1987)115<1083:CSAPOL>2.0.CO;2.

Budikova, D. (2009), Role of Arctic sea ice in global atmospheric circulation: A review, *Global Planet. Change*, *68*(3), 149–163, doi:10.1016/j.gloplacha.2009.04.001.

Cavalieri, D., C. Parkinson, P. Gloersen, and H. J. Zwally (1996), *Sea ice concentrations from Nimbus-7 SMMR and DMSP SSM/I-SSMIS passive microwave data, version 1.1, 1979–2014*, NASA DAAC at the Natl. Snow and Ice Data Cent., Boulder, Colo., doi:10.5067/8GQ8LZQVL0VL. accessed:2016-06-15, updated yearly.

Cavalieri, D. J., and C. L. Parkinson (2012), Arctic sea ice variability and trends, 1979–2010, *Cryosphere*, *6*(4), 881–889, doi:10.5194/tc-6-881-2012.

Chan, D., and Q. Wu (2015), Significant anthropogenic-induced changes of climate classes since 1950, *Sci. Rep.*, *5*, 13487.

Chen, D., and H. W. Chen (2013), Using the Köppen classification to quantify climate variation and change: An example for 1901–2010, *Environ. Dev.*, *6*, 69–79, doi:10.1016/j.envdev.2013.03.007.

Chen, H. W., F. Zhang, and R. B. Alley (2016), The robustness of mid-latitude weather pattern changes due to Arctic sea-ice loss, *J. Clim.*, *29*, 7831–7849, doi:10.1175/JCLI-D-16-0167.1.

Cohen, J., J. Jones, J. Furtado, and E. Tziperman (2013), Warm Arctic, Cold Continents: A common pattern related to Arctic sea ice melt, snow advance, and extreme winter weather, *Oceanography*, *26*(4), 150–160, doi:10.5670/oceanog.2013.70.

Cohen, J., et al. (2014), Recent Arctic amplification and extreme mid-latitude weather, *Nat. Geosci.*, *7*(9), 627–637, doi:10.1038/ngeo2234.

Comiso, J. C. (2011), Large decadal decline of the Arctic multiyear ice cover, *J. Clim.*, *25*(4), 1176–1193, doi:10.1175/JCLI-D-11-00113.1.

Comiso, J. C., C. L. Parkinson, R. Gersten, and L. Stock (2008), Accelerated decline in the Arctic sea ice cover, *Geophys. Res. Lett.*, *35*, L01703, doi:10.1029/2007GL031972.

Dee, D. P., et al. (2011), The ERA-Interim reanalysis: Configuration and performance of the data assimilation system, *Q. J. R. Meteorol. Soc.*, *137*(656), 553–597, doi:10.1002/qj.828.

Eisenman, I. (2010), Geographic muting of changes in the Arctic sea ice cover, *Geophys. Res. Lett.*, *37*, L16501, doi:10.1029/2010GL043741.

Francis, J. A., and S. J. Vavrus (2012), Evidence linking Arctic amplification to extreme weather in mid-latitudes, *Geophys. Res. Lett.*, *39*, L06801, doi:10.1029/2012GL051000.

Francis, J. A., W. Chan, D. J. Leathers, J. R. Miller, and D. E. Veron (2009), Winter Northern Hemisphere weather patterns remember summer Arctic sea-ice extent, *Geophys. Res. Lett.*, *36*, L07503, doi:10.1029/2009GL037274.

Hilmer, M., and T. Jung (2000), Evidence for a recent change in the link between the North Atlantic Oscillation and Arctic Sea ice export, *Geophys. Res. Lett.*, *27*(7), 989–992, doi:10.1029/1999GL010944.

Huang, N. E., and Z. Wu (2008), A review on Hilbert-Huang transform: Method and its applications to geophysical studies, *Rev. Geophys.*, *46*, RG2006, doi:10.1029/2007RG000228.

Huang, N. E., Z. Shen, S. R. Long, M. C. Wu, H. H. Shih, Q. Zheng, N.-C. Yen, C. C. Tung, and H. H. Liu (1998), The empirical mode decomposition and the Hilbert spectrum for nonlinear and non-stationary time series analysis, *Proc. R. Soc. A*, *454*, 903–995.

Johnson, N. C., S. B. Feldstein, and B. Tremblay (2008), The continuum of Northern Hemisphere teleconnection patterns and a description of the NAO shift with the use of self-organizing maps, *J. Clim.*, *21*(23), 6354–6371.

Kim, B.-M., S.-W. Son, S.-K. Min, J.-H. Jeong, S.-J. Kim, X. Zhang, T. Shim, and J.-H. Yoon (2014), Weakening of the stratospheric polar vortex by Arctic sea-ice loss, *Nat. Commun.*, *5*, 4646, doi:10.1038/ncomms5646.

Koenigk, T., M. Caian, G. Nikulin, and S. Schimanke (2016), Regional Arctic sea ice variations as predictor for winter climate conditions, *Clim. Dyn.*, *46*(1–2), 317–337, doi:10.1007/s00382-015-2586-1.

Kohonen, T. (1982), Self-organized formation of topologically correct feature maps, *Biol. Cybern.*, *43*(1), 59–69, doi:10.1007/BF00337288.

Mills, C. M., and J. E. Walsh (2014), Synoptic activity associated with sea ice variability in the Arctic, *J. Geophys. Res. Atmos.*, *119*, 12,117–12,131, doi:10.1002/2014JD021604.

Mwasiagi, J. I. (Ed.) (2011), *Self Organizing Maps—Applications and Novel Algorithm Design*, InTech, Rijeka, Croatia.

Onarheim, I. H., T. Eldevik, M. Årthun, R. B. Ingvaldsen, and L. H. Smedsrud (2015), Skillful prediction of Barents Sea ice cover, *Geophys. Res. Lett.*, *42*, 5364–5371, doi:10.1002/2015GL064359.

Overland, J. E., K. R. Wood, and M. Wang (2011), Warm Arctic-Cold continents: Climate impacts of the newly open Arctic sea, *Polar Res.*, *30*, 15787, doi:10.3402/polar.v30i0.15787.

Pedersen, R. A., I. Cvijanovic, P. L. Langen, and B. M. Vinther (2015), The impact of regional Arctic sea ice loss on atmospheric circulation and the NAO, *J. Clim.*, *29*, 889–902, doi:10.1175/JCLI-D-15-0315.1.

Peings, Y., and G. Magnusdottir (2014), Response of the wintertime Northern Hemisphere atmospheric circulation to current and projected Arctic sea ice decline: A numerical study with CAM5, *J. Clim.*, *27*(1), 244–264, doi:10.1175/JCLI-D-13-00272.1.

Petoukhov, V., and V. A. Semenov (2010), A link between reduced Barents-Kara sea ice and cold winter extremes over northern continents, *J. Geophys. Res.*, *115*, D21111, doi:10.1029/2009JD013568.

Reusch, D. B., and R. B. Alley (2007), Antarctic sea ice: A self-organizing map-based perspective, *Ann. Glaciol.*, *46*(1), 391–396, doi:10.3189/172756407782871549.

Screen, J. A., and I. Simmonds (2010), The central role of diminishing sea ice in recent Arctic temperature amplification, *Nature*, *464*(7293), 1334–1337, doi:10.1038/nature09051.

Screen, J. A., C. Deser, I. Simmonds, and R. Tomas (2013), Atmospheric impacts of Arctic sea-ice loss, 1979–2009: Separating forced change from atmospheric internal variability, *Clim. Dyn.*, *43*(1–2), 333–344, doi:10.1007/s00382-013-1830-9.

Semenov, V. A., and M. Latif (2015), Nonlinear winter atmospheric circulation response to Arctic sea ice concentration anomalies for different periods during 1966–2012, *Environ. Res. Lett.*, *10*(5), 054020, doi:10.1088/1748-9326/10/5/054020.

Simmonds, I. (2015), Comparing and contrasting the behaviour of Arctic and Antarctic sea ice over the 35 year period 1979–2013, *Ann. Glaciol*, *56*, 18–28.

Stroeve, J. C., M. C. Serreze, M. M. Holland, J. E. Kay, J. Malanik, and A. P. Barrett (2012a), The Arctic's rapidly shrinking sea ice cover: A research synthesis, *Clim. Change*, *110*(3–4), 1005–1027, doi:10.1007/s10584-011-0101-1.

Stroeve, J. C., V. Kattsov, A. Barrett, M. Serreze, T. Pavlova, M. Holland, and W. N. Meier (2012b), Trends in Arctic sea ice extent from CMIP5, CMIP3 and observations, *Geophys. Res. Lett.*, *39*, L16502, doi:10.1029/2012GL052676.

Tang, Q., X. Zhang, X. Yang, and J. A. Francis (2013), Cold winter extremes in northern continents linked to Arctic sea ice loss, *Environ. Res. Lett.*, *8*(1), 014036, doi:10.1088/1748-9326/8/1/014036.

Thompson, D., and J. Wallace (1998), The Arctic Oscillation signature in the wintertime geopotential height and temperature fields, *Geophys. Res. Lett.*, *25*(9), 1297–1300, doi:10.1029/98GL00950.

Vihma, T. (2014), Effects of Arctic sea ice decline on weather and climate: A review, *Surv. Geophys.*, *35*(5), 1175–1214, doi:10.1007/s10712-014-9284-0.

Walsh, J. E. (2014), Intensified warming of the Arctic: Causes and impacts on middle latitudes, *Global Planet. Change*, *117*, 52–63, doi:10.1016/j.gloplacha.2014.03.003.

Wu, B., J. Wang, and J. E. Walsh (2006), Dipole Anomaly in the winter Arctic atmosphere and its association with sea ice motion, *J. Clim.*, *19*(2), 210–225, doi:10.1175/JCLI3619.1.

Wu, Q., and X. Zhang (2010), Observed forcing-feedback processes between Northern Hemisphere atmospheric circulation and Arctic sea ice coverage, *J. Geophys. Res.*, *115*, D14119, doi:10.1029/2009JD013574.

Wu, Z., and N. E. Huang (2009), Ensemble empirical mode decomposition: A noise-assisted data analysis method, *Adv. Adapt. Data Anal.*, *1*(1), 1–41, doi:10.1142/S1793536909000047.